

# Open Research Online

---

The Open University's repository of research publications and other research outputs

## Multiscale correlated analysis of the Aguas Zarcas CM chondrite

### Journal Item

#### How to cite:

Dionnet, Zélia; AléonToppani, Alice; Brunetto, Rosario; Rubino, Stefano; Suttle, Martin D.; Lantz, Celine; Avdellidou, Chrysa; Baklouti, Donia; Borondics, Ferenc; Djouadi, Zahia; Greco, Francesco; Héripré, Eva; Nakamura, Tomoki; Rotundi, Alessandra and Scheel, Mario (2022). Multiscale correlated analysis of the Aguas Zarcas CM chondrite. *Meteoritics & Planetary Science* (Early access).

For guidance on citations see [FAQs](#).

© 2022 The Authors



<https://creativecommons.org/licenses/by-nc-nd/4.0/>

Version: Version of Record




Link(s) to article on publisher's website:  
<http://dx.doi.org/doi:10.1111/maps.13807>

---

Copyright and Moral Rights for the articles on this site are retained by the individual authors and/or other copyright owners. For more information on Open Research Online's data [policy](#) on reuse of materials please consult the policies page.

---

## Multiscale correlated analysis of the Aguas Zarcas CM chondrite

Zélia DIONNET <sup>1,2,3,\*</sup>, Alice ALÉON-TOPPANI <sup>1</sup>, Rosario BRUNETTO<sup>1</sup>, Stefano RUBINO<sup>1</sup>, Martin D. SUTTLE <sup>4</sup>, Cateline LANTZ<sup>1</sup>, Chrysa AVDELLIDOU<sup>5</sup>, Donia BAKLOUTI<sup>1</sup>, Ferenc BORONDICS<sup>6</sup>, Zahia DJOUADI<sup>1</sup>, Francesco GRECO<sup>7</sup>, Eva HÉRIPRÉ<sup>8</sup>, Tomoki NAKAMURA<sup>9</sup>, Alessandra ROTUNDI<sup>2,3</sup>, and Mario SCHEEL<sup>6</sup>

<sup>1</sup>Institut d'Astrophysique Spatiale, CNRS, Université Paris-Saclay, Orsay 91405, France

<sup>2</sup>Dip. Di Scienze Applicate, Università di Napoli Parthenope, Centro Direzionale di Napoli, Isola C4, Naples 80143, Italy

<sup>3</sup>Istituto di Astrofisica e Planetologia Spaziali—INAF, Rome, Italy

<sup>4</sup>School of Physical Sciences, The Open University, Walton Hall, Milton Keynes MK7 6AA, UK

<sup>5</sup>Observatoire de la Côte d'Azur, Laboratoire Lagrange, CNRS, Université Côte d'Azur, Blvd de l'Observatoire, Nice Cedex 4 06304, France

<sup>6</sup>SOLEIL Synchrotron, Gif-sur-Yvette, France

<sup>7</sup>Department of Physics and Astronomy, University of Ghent, Ghent, Belgium

<sup>8</sup>CentraleSupélec, CNRS, Laboratoire de Mécanique des Sols, Université Paris-Saclay, Structures et Matériaux, Gif-sur-Yvette 91190, France

<sup>9</sup>Division of Earth and Planetary Materials Science, Laboratory for Early Solar System Evolution, Tohoku University, Sendai, Japan

\*Corresponding author: E-mail: zelia.dionnet@universite-paris-saclay.fr

(Received 09 October 2021; revision accepted 21 February 2022)

---

**Abstract**—In this paper, we report the results of a campaign of measurements on four fragments of the CM Aguas Zarcas (AZ) meteorite, combining X-ray computed tomography analysis and Fourier-transform infrared (FT-IR) spectroscopy. We estimated a petrologic type for our sampled CM lithology using the two independent techniques, and obtained a type CM2.5, in agreement with previous estimations. By comparing the Si-O 10- $\mu$ m signature of the AZ average FT-IR spectra with other well-studied CMs, we place AZ in the context of aqueous alteration of CM parent bodies. Morphological characterization reveals that AZ has heterogeneous distribution of pores and a global porosity of  $4.5 \pm 0.5$  vol %. We show that chondrules have a porosity of  $6.3 \pm 1$  vol%. This larger porosity could be inherited due to various processes such as temperature variation during the chondrule formation and shocks or dissolution during aqueous alteration. Finally, we observed a correlation between 3D distributions of organic matter and mineral at micrometric scales, revealing a link between the abundance of organic matter and the presence of hydrated minerals. This supports the idea that aqueous alteration in AZ's parent body played a major role in the evolution of the organic matter.

---

### INTRODUCTION

CM chondrites are the most abundant samples among carbonaceous chondrites and hydrated meteorite (Suttle et al., 2021). There is significant diversity among CM chondrites as they exhibit evidence of varying degrees of aqueous alteration and brecciation (Brearley, 2013; Brearley & Jones, 1998; Chizmadia & Brearley, 2008; Metzler et al., 1992). Thus, they represent very valuable sources to understand the mechanisms involved

in aqueous alteration and the nature of alteration products (e.g., Hanowski & Brearley, 2001; Hewins et al., 2014). Aguas Zarcas (AZ) is a recent CM fall recovered from Costa Rica in 2019. Thanks to a rapid recovery, hundreds of fragments were collected before local rainfall. This makes the samples from this carbonaceous chondrite very valuable because terrestrial alteration is highly limited, as proven by a fresh fusion crust (Martin & Lee, 2020) and the absence of common weathering products. This chondrite is classified as a

CM2 breccia in the Meteoritical Bulletin (Gattacceca et al., 2019). In 2020, several groups presented the results of preliminary characterizations and analyses of several fragments of AZ (Davidson et al., 2020; Hicks & Bridges, 2020; Kebukawa et al., 2020; Kouvatsis & Cartwright, 2020; Pizzarello et al., 2020; Takir et al., 2020; Tunney et al., 2020; Villalon et al., 2020) describing at least three main lithologies: one rich in metal and two CM lithologies, including a chondrule-rich and a chondrule-poor variety.

More recently, Kerraouch et al. (2021) described five different lithologies, reflecting the petrographic diversity of materials preserved in the AZ meteorite. They distinguished a brecciated CM lithology, a C1/2 lithology, a C1 lithology, and two distinct metal-rich lithologies. According to them, the presence of multiple lithologies and their intricacy at millimetric scale as well as the presence of unique and rare lithologies in AZ indicates a complex history in a “highly dynamic environment.” Thus the history of AZ could be comparable to the history of the rubble-pile asteroids Ryugu and Bennu, which are interpreted as second-generation parent bodies, formed by disruption and reaccretion (Michel et al., 2020; Okada et al., 2020; Walsh et al., 2020). The recent discovery of pyroxene brecciated boulders on the surface of Bennu has confirmed this hypothesis (DellaGiustina et al., 2021). Kerraouch et al. (2021) concluded that “the different lithologies of the fresh AZ breccia, which represent different levels of hydration and heating, are good analogs for the types of materials that will be returned from asteroids Bennu and Ryugu.” More recently, analyses of Ryugu grains have shown that their spectra are different from the ones of CM meteorites and more similar to the ones of CI chondrites (Pilorget et al., 2021; Yada et al., 2021). However, the remote sensing spectrum of asteroid Bennu measured by the OTES instrument onboard OSIRIS-REx (Hamilton et al., 2021) has shown that Bennu is closer to CM chondrites. This makes the AZ meteorite, and more generally fresh CM chondrites, high priority samples for further investigation.

The mineralogy of AZ has been described in several abstracts (see Hicks & Bridges, 2020; Takir et al., 2020). They have described abundant phyllosilicate (mainly serpentine) mixed with olivine and pyroxene grains and FeNi sulfides. Some groups have also shown that the organic matter contained in AZ is also intriguing (Pizzarello et al., 2020; Tunney et al., 2020). According to Kebukawa et al. (2020), the organic compounds present inside the metal-rich lithologies are unique with high aliphatic concentrations, indicating a more primitive nature relative to the organic matter found in a “typical” CM lithology. However, they described this CM-like lithology as very comparable to that measured from Murchison. Likewise, Glavin et al. (2021) studied

the amino acids and found similar properties to those measured in Murchison. The heterogeneity of the organic matter, resulting from very different postaccretional histories, inside a single meteorite reinforces the idea of a complex history with reagglomeration, as presented by Kerarouch et al. (2021) inside AZ, and inside other carbonaceous chondrites (Changela et al., 2018; Le Guillou et al., 2014, Vinogradoff et al., 2017). Therefore, multiscale correlated analysis of the different lithologies within the AZ meteorite has the potential to unlock new insights into the interaction between silicate rock and organics on primitive C-type asteroids.

In this paper, we report the results of a multianalytical campaign on four fragments of different sizes from the AZ meteorite. In the first section, we present the results of a synchrotron-based X-ray computed tomography (XCT) characterization on a millimetric fragment of AZ to explore the structural diversity of this meteorite. The XCT data also allowed us to calculate the microporosity of AZ. We then describe Fourier-transform infrared (FT-IR) reflection measurements on a millimetric fragment of AZ to get a large-scale first look at its molecular composition and to obtain the average AZ spectrum, which can be compared to remote sensing observation of asteroid surfaces (Hamilton et al., 2021; Kitazato et al., 2019). Finally, we performed complementary measurements on two small fragments of AZ by FT-IR hyperspectral imaging, to study organic matter and characterize the mineral phases at a higher spatial resolution (1–100  $\mu\text{m}$ ). In the Discussion section, we combined information obtained from FT-IR and X-ray imaging over a wide range of length scales from the millimeter scale down to the micron scale, and used these to discuss different stages of AZ’s history.

## MATERIALS AND METHODS

### Sample Description and Analytical Plan

At the Institut d’Astrophysique Spatiale (IAS), we obtained a mm-sized fragment of AZ with a mass of approximately 0.15 g. Four fragments of different sizes were extracted from this large fragment and analyzed by different analytical methods requiring different preparation. Table 1 summarizes the characteristics of the four studied fragments, while a more complete description of each fragment and the associated analysis is given below. Note that AZ-3 sections are focused ion beam (FIB) sections that were extracted from fragment AZ\_3.

First of all, FT-IR imaging analysis in reflection mode was performed on a small part of the surface of the largest fragment (AZ\_1) (Fig. 1). The AZ\_1

TABLE 1. Inventory of AZ fragments studied in this work, including details of the different analytical methods and fragment preparation procedures used.

Name	Size	Applied measurement	Sample preparation
AZ_1	Surface: $300 \times 300 \mu\text{m}$	FT-IR-reflection	Raw fragment
AZ_2	$1160 \times 920 \times 400 \mu\text{m}$	X-CT	Raw fragment
AZ_3	$20 \times 15 \times 30 \mu\text{m}$	FT-IR-reflection + IR-CT	Welded on W needle
AZ_3_sections	$2 \mu\text{m}$ thin	FT-IR-2D transmission + Raman + EDS	FIB sections of AZ_3
AZ_4	$200 \times 200 \times 11 \mu\text{m}$	FT-IR-2D transmission	Crushed inside diamond cell

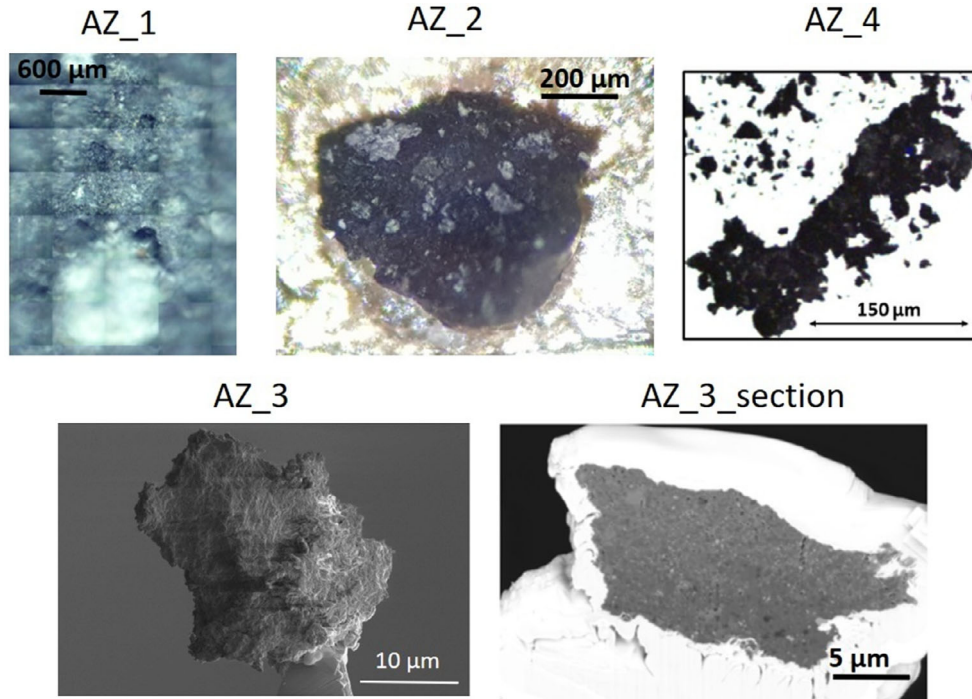


Fig. 1. Optical images (for AZ\_1, AZ\_2, and AZ\_4) and SEM images (for AZ\_3 and AZ\_3\_section) of the fragments of the AZ meteorite studied in this paper.

fragment was later subsampled using a scalpel, generating a smaller chip (AZ\_2:  $1160 \mu\text{m} \times 920 \mu\text{m} \times 400 \mu\text{m}$  size), which was then analyzed by XCT.

A first micrometric fragment AZ\_3 ( $20 \times 15 \times 30 \mu\text{m}^3$ ) was then analyzed using 3D FT-IR hyperspectral imaging to study the 3D distribution of the different phases. This fragment was naturally detached from the bulk (neither selection nor preparation). It was welded onto the tip of a tungsten needle by platinum ion beam-induced deposition (as in Aléon-Toppiani et al., 2021). Measurements in reflection at different angles were first acquired on the small fragment AZ\_3 to obtain data on the fragment's surface composition. We then performed FT-IR tomography (see Dionnet, Brunetto, et al. [2020] for a description of the method) to analyze the abundance and 3D distribution of mineral phases and organic matter inside

the fragment while preserving its physical integrity. Thanks to this 3D characterization, we were able to visualize the compositional heterogeneity inside the fragment and subsequently select specific areas to study at higher resolution. We then extracted three FIB sections ( $3 \mu\text{m}$  thickness) from the AZ\_3 fragment by using FIB preparation, and performed FT-IR and Raman microspectroscopy on them (see Aléon-Toppiani et al. [2021] for the description of the full protocol on a 3D fragment to FIB sections).

The FIB sections were later analyzed by energy-dispersive X-ray spectroscopy (EDS) in a scanning electron microscope (SEM) to retrieve the structure and elemental composition. These analyses at smaller scales are well adapted for studying the carbonaceous component and its mineral host, down to the micrometer scale (Aléon-Toppiani et al., 2021).

Finally, another micrometric fragment AZ\_4 was analyzed using a more invasive and classical preparation: fragment AZ\_4 was crushed inside a diamond compression cell (as in Merouane et al. [2012] and in Dionnet et al. [2018]), forming a flattened sample with a thickness of  $\sim 11 \mu\text{m}$  and a surface area below  $200 \times 200 \mu\text{m}$ . In such preparation, we lose information about the 3D structure but we maximize the IR response of the organic and mineral signatures in transmission by reducing scattering effects.

### XCT Analyses: Measurement and Data Treatment

XCT measurements were performed at the synchrotron SOLEIL (France) on the ANATOMIX beamline (Weitkamp et al., 2017) for fragment AZ\_2, with a monochromatic beam at 16.87 keV and a voxel size of  $0.325 \mu\text{m}$  for a field of view of  $0.65 \text{mm}^2$ . Thanks to X-ray 2D detectors, we measured 2000 projections that were normalized using corresponding flat- and dark-field images. The filtered projections allow reconstruction of a 3D volume using ring filters (Paganin et al., 2002) by means of the academic software PyHST2 (Mirone et al., 2014). The voxel value in the 3D volume corresponds to the linear attenuation coefficient (LAC) of the material.

The LAC gives indications about the average atomic number of the probed matter, meaning that features with high-density contrast, such as pores, can be quickly resolved. First, we segmented our data using a LAC threshold that discriminates two components: pores versus silicate phases. A more detailed description of this method is presented by Dionnet, Suttle, et al. (2020). After data segmentation, we measured the porosity by counting the number of empty voxels inside the fragment divided by the number of voxels composing the fragment. These data also allowed us to study the size and the shape distributions of the different populations of voids with a resolution around  $1 \mu\text{m}$ . The study of pore anisotropy employed the Quant3D software (Ketcham, 2005; Ketcham & Ryan, 2004).

We then performed a more complex segmentation. As suggested by Griffin et al. (2012), features inside a CM chondrite can be identified using segmentation based on the surrounding voxels' average value. In this study, for each silicate-voxel, we generated the histogram of the LAC value for a square of  $20 \times 20$  voxels around the voxel of interest. We then estimated the mean and the standard deviation of this distribution and used these values to classify the voxel. Finally, based on knowledge of CM chondrites (Howard et al., 2015) and previous studies of AZ, we are able to identify regions with different LAC values as common

components inside CM chondrites. For instance, chondrules correspond to darker areas with a quite large standard deviation, by contrast, tochilinite-cronstedtite intergrowths (TCIs) can be identified as bright areas with a very small dispersion of the LAC distribution. Thanks to this second segmentation, we have estimated volume proportions of the chondrules and the TCIs within the matrix.

A manual inspection helped us to determine specific parameters on a few chondrules. First, we extracted their size and morphological properties. We then performed 3D analyses of small regions around some representative chondrules. We obtained the chondrule's volume, a description of its shape, and the values of their porosities. All the 3D models presented in this article have been produced thanks to the software Tomviz (tomviz.org).

### FT-IR Spectroscopy

FT-IR hyperspectral imaging was performed on the surface of AZ\_1, on the two smaller fragments AZ\_3 and AZ\_4, and on the AZ\_3 sections with an Agilent Cary 670/620 microspectrometer coupled to a focal plane array (FPA) detector of  $128 \times 128$  pixels, installed at the SMIS beamline of the SOLEIL synchrotron. Each pixel collects a whole spectrum in the range  $850\text{--}3950 \text{cm}^{-1}$  ( $\sim 2.5$  to  $11.8 \mu\text{m}$ ). Before each analysis, we collected a background using either a gold standard for the reflectance measurements, or a close empty point inside the diamond compression cell for the transmittance measurements on the needle-mounted fragment. We used the internal Globar source for all the analyses presented in this paper, while in all measurements, the spatial resolution was diffraction-limited (for details, see Dionnet et al., 2018; Sandt et al., 2019).

Representative areas on the surface of the grain AZ\_1 were analyzed in reflectance with a  $\times 15$  objective at standard magnification (which provides a  $5.5 \mu\text{m}$  projected pixel size) with a spectral resolution of  $4 \text{cm}^{-1}$ .

For the fragment AZ\_3, we acquired a collection of hyperspectral maps in 2D for the fragment mounted at the tip of the tungsten needle. When rotating the fragment, a 2D hyperspectral map in reflectance was acquired every  $20^\circ$  with a pixel size of  $3.3 \mu\text{m}$  ( $\times 25$  objective in standard magnification mode) and a spectral resolution of  $8 \text{cm}^{-1}$ . These 2D hyperspectral reflectance maps can be projected on a 3D shape model obtained from the high resolution images collected in the SEM at different angles, providing a novel technique of combining FT-IR and SEM images in 3D,

never used before on an extraterrestrial material. This task is done by comparing and aligning the projections of the SEM 3D model with the infrared reflectance maps. Prominent localized topological or spectral features are used to strengthen the spatial correlation.

The AZ\_4 fragment flattened in the compression cell was analyzed in transmittance with the same objective lens ( $\times 25$ ) but also employing additional high magnification optics, i.e., with an additional  $\times 5$  magnification placed in front of the FPA detector. This gives a  $0.66 \mu\text{m}$  projected pixel size. Here our spectral resolution was  $4 \text{ cm}^{-1}$ . A similar configuration was used to analyze the FIB sections extracted from the second micrometric grain (AZ\_3).

Finally, for the infrared computed tomography (IR-CT) measurements (Yesiltas et al., 2016), we collected 180 2D hyperspectral maps (projections) in transmission with a pixel size of  $0.66 \mu\text{m}$  ( $\times 25$  objective in high magnification mode) and a spectral resolution of  $4 \text{ cm}^{-1}$  (for further details, see the method described by Dionnet, Brunetto, et al., 2020).

### Raman Microspectroscopy

We acquired Raman spectra on the three FIB sections extracted from the fragment AZ\_3, in order to characterize the aromatic component of their organic matter and to determine AZ's organic heterogeneity. The Raman spectrometer used was a Thermo Fisher with a  $532 \text{ nm}$  exciting laser radiation. Maps on the FIB sections were recorded with a laser spot through an Olympus UIS2 100X/0.90 NA LWD objective providing a spot size of about  $1 \mu\text{m}$ . The laser power was less than  $0.3 \text{ mW}$ , similar to previous studies on the Paris meteorite (Dionnet et al., 2018) in order to avoid any laser-induced damage to the samples.

### SEM-EDS Analysis

In addition to secondary electron images, some quantitative analyses were also performed on AZ\_3 FIB sections with EDS on a SEM. SEM-EDS acquisitions were done at  $20 \text{ keV}$  on a Thermo Fisher HELIOS Nanolab 660 dual beam microscope fitted with an EDAX Octane super  $30 \text{ mm}^2$  EDS analytical system. These analyses were used to extract the ratio Mg/Fe on few locations inside FIB sections. SE images have been analyzed to extract porosity with a resolution of  $0.1 \mu\text{m}$  thanks to the threshold method using ImageJ. The choice of the threshold and saturation of the sample due to charging effects are the main errors sources. The estimation of the porosity is thus obtained with a relative error of 15%.

## RESULTS

### XCT Analyses: Morphological Description at the Large Scale

#### *Global Description of the Morphological Properties*

Fragment AZ\_2 is very heterogeneous, showing a complex assembly of minerals with different LAC and thus various compositions. The main structures are identified in Fig. 2. We can distinguish two main distinct components, which most likely correspond to different lithologies:

- (i) Most of the fragment has a texture similar to the one described in the CM-lithology of AZ (Kerrouach et al., 2021). Based on this previous study and expected composition of CM chondrites (Howard et al., 2015), we have inferred the identification of the different components visible in XCT images. Indeed, Fig. 2 reveals the presence of many structures embedded inside a fine-grained matrix (Howard et al., 2015; Kerrouach et al., 2021; Leroux et al., 2015).

The fragment AZ\_2 contains a lot of bright rounded regions. These regions have a higher LAC than the matrix, as they contain more iron. They are interpreted as TCIs, which are common features in CM chondrites that have experienced mild to moderate degrees of aqueous alteration (Rubin et al., 2007). Previously, Martin and Lee (2020) also noticed the presence of numerous TCIs in the matrix of AZ. Using the segmentation procedure, we determine that TCIs represent 26 vol% of the CM-like lithology in this fragment. This value is consistent with the expected values for CM chondrites (i.e., between 15 and 40 vol%; Rubin et al., 2007).

Few chondrules are present in this fine-grained matrix. Thanks to the second segmentation protocol, we calculate the relative chondrule abundance as  $17 \pm 2 \text{ vol\%}$  in the CM-like lithology. This value with its error bar fits with the estimation presented in Kouvatzis and Cartwright (2020) that chondrules represent around 16 vol% in the chondrule-poor CM lithology. This indicates that the majority of our large fragment comes from the chondrule-poor CM lithology as defined in Kouvatzis and Cartwright (2020).

In addition, we noticed a few multiphase regions, with irregular shapes, enclosed in fine-grained rims. We identified them as possible CAIs. We detected only a few metallic Fe-Ni bearing phases, which is consistent with the SEM-EDS observations performed by Martin and Lee (2020) for lithologies present inside our fragment. Material related to the two metal-rich lithologies identified by Kerraouch et al. (2021) is absent in this fragment.

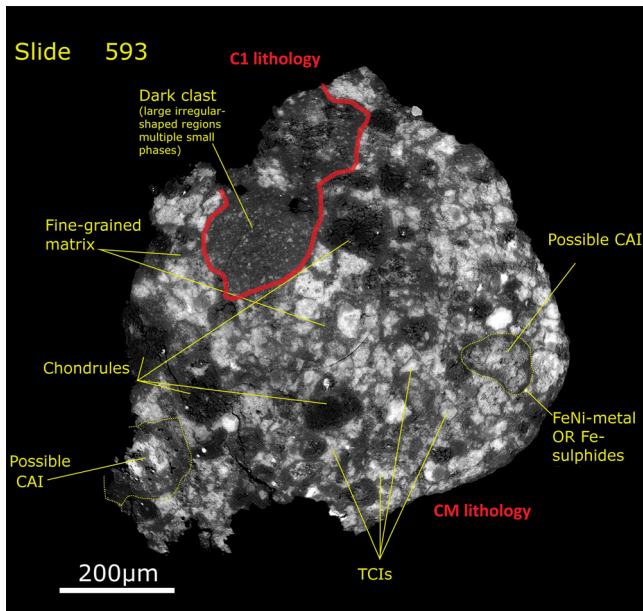


Fig. 2. XCT slice inside the fragment AZ\_2 with identification of different components.

(ii) The second lithology is present in AZ\_2 as a small region, visible in the top left of Fig. 2. This lithology has a relatively homogeneous texture at the  $\mu\text{m}$  scale and contains some bright inclusions. Its texture is somewhat similar to that of chondrule fine-grained rims. By comparing our data and XCT data published in Kerraouch et al. (2021), we identify this part of the fragment as a clast coming from the C1 lithology, representing 6.5 vol% of the fragment AZ\_2. This lithology is composed of matrix phyllosilicates, magnetite, sulfides, and some carbonates (Kerraouch et al., 2021).

### Study of Porosity

Our estimation of the porosity inside AZ\_2 gave a value of  $4.5 \pm 0.5$  vol% at a voxel size of  $0.325 \mu\text{m}$ . This is similar to porosity values estimated for CMs with image analysis methods (Corrigan et al., 1997). A striking feature of our fragment is that pores are not equally distributed, as illustrated in Fig. 3, where the pores are colored in red. We can distinguish areas with many pores (as for instance the lower left of the fragment presented in Fig. 3) and in contrast, we can also find regions with almost no pores (mainly matrix far from any chondrules or fractures). In the fragment AZ\_2, a large proportion of pores (44 vol%) are located near/in chondrules, but only represent 6.5 vol% of the whole fragment.

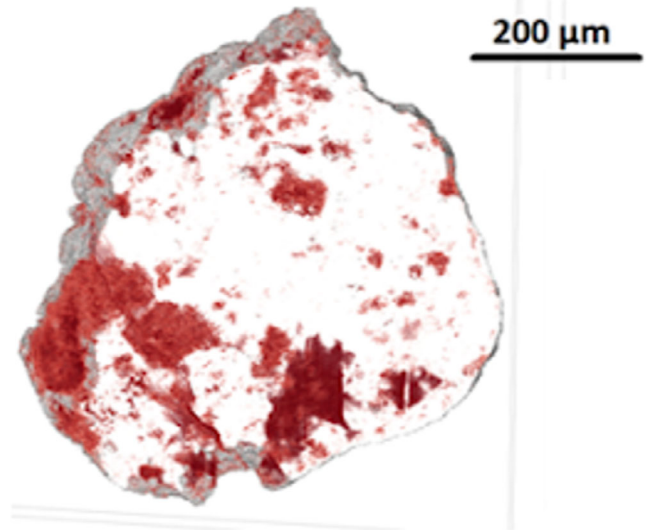


Fig. 3. 3D visualization of half the fragment of AZ\_2 (sliced in the middle), with the pores emphasized in red and the edges in gray. The figure allows the visualization of all the pores present in the half fragment.

### Study of Chondrules

A manual identification of 12 porphyritic/granular chondrules was performed to more precisely characterize physical parameters such as chondrule shape, size, and anisotropy. These chondrules have diameters between 40 and  $400 \mu\text{m}$ , which is consistent with the observation of Kouvatzis and Cartwright (2020). Moreover, collection of 3D data facilitated the accurate study of their shape. We observed that chondrules generally have a moderate elongated shape: average anisotropic index  $A = 4.25$  (an anisotropic coefficient of 1 means spherical shape and the larger is the value of  $A$ , the more elongated are the studied components). However, we did not observe any preferred orientation of the elongation direction.

Finally, we determined an average porosity of  $6.3 \pm 1$  vol% inside the chondrules, which varies among individual chondrules: with low values inside smaller chondrules (as the one shown in Fig. 4b) and higher values inside chondrules that are located near fractured regions (see Fig. 4a). Some chondrules present internal elongated pores as in Fig. 4c, not associated with fractures inside the whole fragment. The pores inside chondrules are elongated with an anisotropic coefficient of  $A = 6.25$ . Notably, pores inside elongated chondrules often follow the direction of the elongation of their respective chondrule. As a point of comparison, we also estimated the anisotropy coefficient of pores

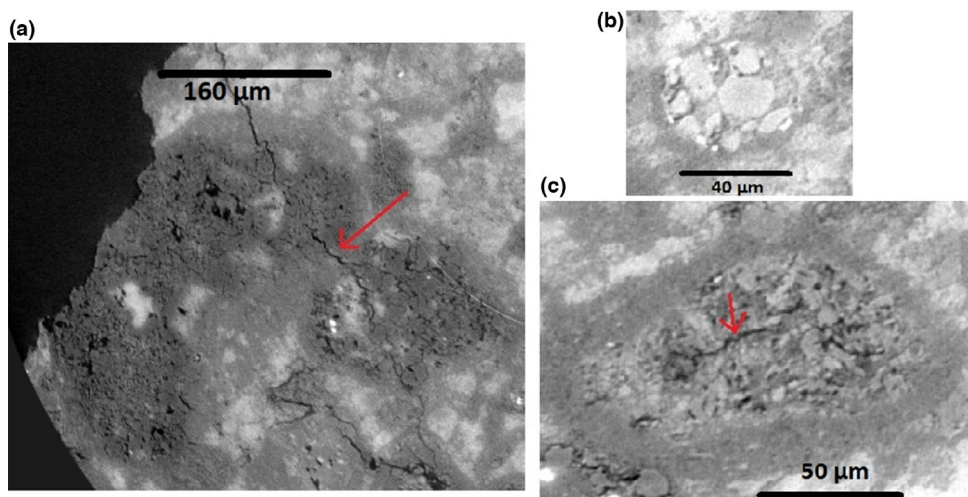


Fig. 4. XCT images of representative chondrules inside CM's lithology inside the fragment AZ\_2. The arrows indicate elongated fractures inside or near chondrules.

present inside the matrix ( $A = 11.3$ ). This very high value means that pores detected in this study (at the micrometric scale) are mainly present in the form of long cracks inside the matrix.

#### FT-IR Spectroscopy in Reflection: Mineral Components and Their Heterogeneity

We conducted two multiscale campaigns using FT-IR hyperspectral imaging. The following section presents the results we obtained in reflectance at the surface of the large fragment (AZ\_1) and on the small 3D fragment (AZ\_3). We have performed this study to characterize the mineral components and their heterogeneity. Moreover, spectra obtained in reflectance are valuable as they are comparable to remote sensing data.

#### Average Mid-Infrared Spectra at Large Scale

The large chip (grain AZ\_1) was analyzed in reflection with a  $\times 15$  objective in order to obtain FT-IR spectra representative of the whole fragment. The average spectrum of the matrix was obtained by averaging 16,384 spectra, corresponding to an area of  $700 \mu\text{m} \times 700 \mu\text{m}$ . Moreover, another area was analyzed at the edge of a chondrule to obtain the spectra of a large chondrule (this chondrule has a diameter around  $800 \mu\text{m}$ ) and this time, we averaged the 76 spectra corresponding to the big chondrule. Both spectra are presented in Fig. 5.

The mid-infrared (MIR) spectra (Fig. 5a) can be divided into two parts, affected by different scattering

regimes. The Christiansen feature, around  $1100 \text{ cm}^{-1}$  ( $\sim 9.1 \mu\text{m}$ ), marks the boundary between the surface scattering regime for higher wavelengths and the volume scattering regime for lower wavelengths. The main retstrahlen band is centered around  $1000 \text{ cm}^{-1}$  ( $10 \mu\text{m}$ ) and is related to the Si-O stretching modes of silicates. In the average spectra of the matrix, we observed a broad band centered around  $1000 \text{ cm}^{-1}$  ( $10 \mu\text{m}$ ). At high wave numbers, we observe a large band due to water stretching mode between  $3000$  and  $3700 \text{ cm}^{-1}$  with a small shoulder due to OH at  $3660 \text{ cm}^{-1}$  ( $\sim 2.7 \mu\text{m}$ ). Measurements were performed under ambient air and a part of the detected water is due to adsorbed water. This contribution is an issue for quantitative study of water but does not affect quantitative comparison of various regions inside a single sample as discussed below.

In hydrated carbonaceous chondrites, the OH band is typical of phyllosilicates (Beck et al., 2014). Water bending modes are responsible for a weak band at  $1640 \text{ cm}^{-1}$  ( $\sim 6.1 \mu\text{m}$ ). As described in Beck et al. (2014), the  $10 \mu\text{m}$  profile in our average spectra is similar to a saponite profile, whereas the main expected component of CM carbonaceous chondrites is serpentine as discussed by Howard et al. (2015). Beck et al. (2014) hypothesized that the saponite-like profile for serpentine in CM could be due to (i) serpentine having especially low crystallinity, which impacts the infrared spectra; or (ii) it could be due to the effect of cation substitutions in the serpentines. Thus, we also conclude that in our spectra the large broad band is attributed to serpentine.

On the contrary, the spectra from the chondrule reveal a multip peaked band, with a main peak at



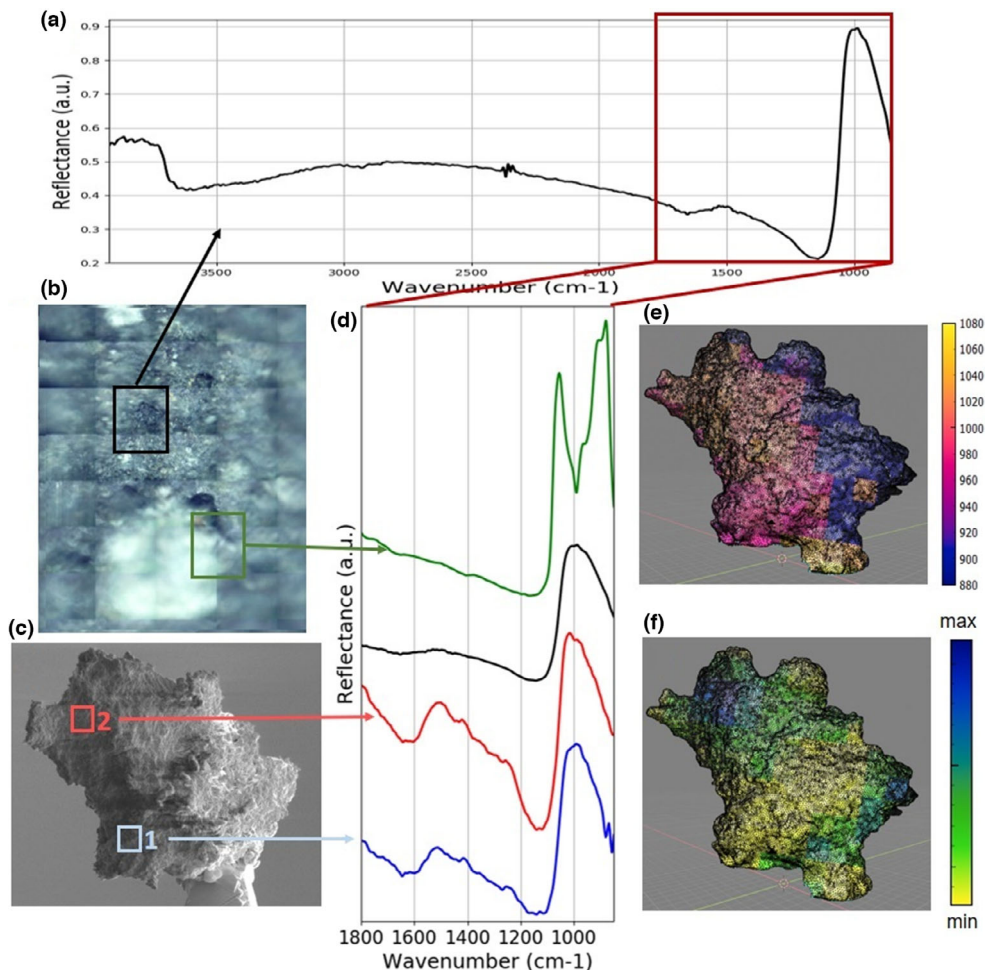


Fig. 5. a) Average FT-IR spectrum of the measured chip surface AZ\_1. b) Visible image of the fragment AZ\_1. c) SEM images of the 3D small fragment AZ\_3. d) Zoom of reflectance spectra in the range 1800–850  $\text{cm}^{-1}$  for the average spectrum in black, inside a chondrule in green and for areas 1 and 2 of panel (c) in red and blue. e) Projection of the SiO band position on the 3D volume: regions in pink and yellow correspond, respectively, to a maximum of the SiO band around 980 and 1010  $\text{cm}^{-1}$ . A part of the fragment was slightly out of focus for this angle and produced a noisier spectrum (blue region in panel [e]). f) Intensity of the H<sub>2</sub>O bands at 1614  $\text{cm}^{-1}$  distribution projected on the 3D volume: more hydrated areas appear in blue and less hydrated ones in yellow.

1056  $\text{cm}^{-1}$  ( $\sim 9.5 \mu\text{m}$ ), a smaller shoulder at 965  $\text{cm}^{-1}$  ( $\sim 10.4 \mu\text{m}$ ), and a strong contribution at 874  $\text{cm}^{-1}$  ( $\sim 11.4 \mu\text{m}$ ), which corresponds to a composition dominated by anhydrous olivine (Hamilton, 2010).

In addition, on the matrix spectra, we also observed very weak contributions of CH features around 2900 and 3000  $\text{cm}^{-1}$  ( $\sim 3.4$  to  $3.3 \mu\text{m}$ ) for the stretching modes and between 1200 and 1400  $\text{cm}^{-1}$  ( $\sim 8.3$  to  $7.1 \mu\text{m}$ ) for CH bending vibrations and aromatic C = C stretching vibrations. Organic matter is more visible in IR transmission and thus a more precise characterization will follow in FT-IR hyperspectral imaging in transmission: organic component and its heterogeneity. Even if aliphatic organic matter is expected to be present in the AZ's spectra, terrestrial

contamination cannot be totally excluded. Indeed, a study on powders has shown that CH features in reflectance could also be attributed to contamination by volatile hydrocarbons induced by exposure to air in the laboratory (Salisbury et al., 1991). It is difficult to conclude based only on the average spectra presented in Fig. 5. Hyperspectral imaging in transmission discussed later will help to remove this ambiguity about the indigenous or exogenous origin of aliphatic matter.

### 3D Studies in Reflection on Preserved Fragments

Reflectance spectra were also collected on the 3D, topographically complex surfaces of the small fragment AZ\_3 (as shown in Fig. 5c in a SEM image of the

fragment). These spectra show large bands of Si-O, typical of phyllosilicate. Their band centers vary between  $980\text{ cm}^{-1}$  ( $\sim 10.2\ \mu\text{m}$ ) and  $1010\text{ cm}^{-1}$  ( $\sim 9.9\ \mu\text{m}$ ) in different areas of the fragments (see Fig. 5e). Figure 5f shows the heterogeneity in terms of hydration at the surface of the fragment AZ\_3. We notice the presence of a more hydrated area at the top of the fragment, which correlates with a small shift of the silicate band position toward larger wavelengths (see area 2 in Fig. 5c).

### FT-IR Hyperspectral Imaging in Transmission: Organic Component and Its Heterogeneity

Reflectance measurements are quite sensitive to inorganic silicate phases and therefore provide information on the identity and diversity of mineral phases. Here, using transmission IR spectroscopy, we are able to collect complementary information on the organic phases and their relationship to the mineralogy in two of the smaller fragments (AZ\_3 and AZ\_4) extracted from the CM-like lithology.

### 3D Studies in Transmission on Preserved Fragments

We performed IR-CT on the small fragment AZ\_3. This technique allows us to analyze the fragment's internal composition. Figures 6b–d show the reconstructed area under different bands in the FT-IR spectra, which are proportional to the volume concentration of different components (for more details on IR-CT, see Dionnet, Brunetto, et al. 2020). The continuum represents the distribution of the matter and brings constraints about the shape of the sample. It is represented in panels b–d in light pink to help the reader to recognize the different components inside the whole sample.

The two bands representative of the distribution of  $\text{H}_2\text{O}$  (around  $1620\text{ cm}^{-1}$  [ $\sim 6.2\ \mu\text{m}$ ] and  $3700\text{ cm}^{-1}$  [ $\sim 2.7\ \mu\text{m}$ ] for the bending and stretching mode, respectively) are shown in blue. The OH band at  $3660\text{ cm}^{-1}$  due to the hydroxyl is visible as a shoulder on the spectra (especially in the blue spectra of Fig. 6). As in reflection, we found a region at the top of the fragment that is more hydrated. The same area is also enriched in aliphatic organic matter, as shown by the orange distribution presented in panel (c) of Fig. 6. The heterogeneity and more clearly the detection of aliphatic organic matter inside the sample by IR-CT (and not only on the surface) are pieces of evidence of the endogenous origin of the majority of organic matter detected in our analyses. This analysis has emphasized a compositional heterogeneity inside the small fragment AZ\_3 and thus we decided to further explore this heterogeneity as described in the following section.

### Analysis of the FIB Sections

The IR-CT 3D measurements have the advantage of being totally nondestructive and noninvasive; however, they are time-consuming (typically 1/2 days per sample) and because of complex scattering issues, the quality of the spectral data in 3D is not as good as equivalent measurements collected in 2D on a flat surface. To overcome this problem, we applied one more step in the sample preparation (see also Aléon-Toppani et al. [2021] for further technical information). The AZ\_3 fragment was serially sectioned using FIB technologies to generate a series of three FIB sections (see Fig. 7a). The orientation of the particle prior to sectioning was carefully selected to ensure that regions of interest were subsampled as required. Thickness of the FIB sections allowed us to perform FT-IR characterization in transmission with a pixel size of  $0.66\ \mu\text{m}$  (without being limited by the scattering effect due to the volume) and also to subsequently measure these same sections with Raman spectroscopy, EDS analysis (see Fig. 7 for an example of the results of the analysis performed on the second sections, located in the middle of the fragment AZ\_3).

The 2D spectra of the FIB sections show bands that are similar to the ones measured in 3D in the whole fragment AZ\_3, but their peak position and their relative band area show small variations between the three sections and between different spots within a single section. In particular, organic matter bands are more important on sections 1 and 2 and located on half of the sections (near areas 2 and 3) as predicted by our 3D characterization. Moreover, we observed a shift of the maximum of the silicate band between  $980\text{ cm}^{-1}$  ( $\sim 10.2\ \mu\text{m}$ ) and  $1010\text{ cm}^{-1}$  ( $\sim 9.9\ \mu\text{m}$ ), both visible in the spectra presented in Fig. 6 and in panel c of Fig. 7. Local variations in Mg/Fe ratio may explain this band shift, as confirmed by the EDS analysis shown in Fig. 7. We have estimated a Mg/Fe ratio of 0.58 for area 1, 1.61 for area 2, and 0.84 for area 3 (both compatible with a serpentine composition). The region enriched in Mg (area 2) corresponds to the region with a maximum of the SiO band around  $1010\text{ cm}^{-1}$  ( $\sim 9.9\ \mu\text{m}$ ). Thus the  $10\ \mu\text{m}$  band detected in our samples shifts toward a higher wave number when the Mg/Fe ratio increases, as previously shown in other solid solution series minerals by Tarantino et al. (2003), Hofmeister and Pitman (2007), Hamilton (2010), and Bates et al. (2020).

Variations in the abundance of organic matter (up to a factor of 3 compared to the average abundance in the whole fragment AZ\_3) or degree of hydration are also visible within the sections (as shown in panels d and e of Fig. 7), i.e., at a scale below  $10\ \mu\text{m}$ . The relationship

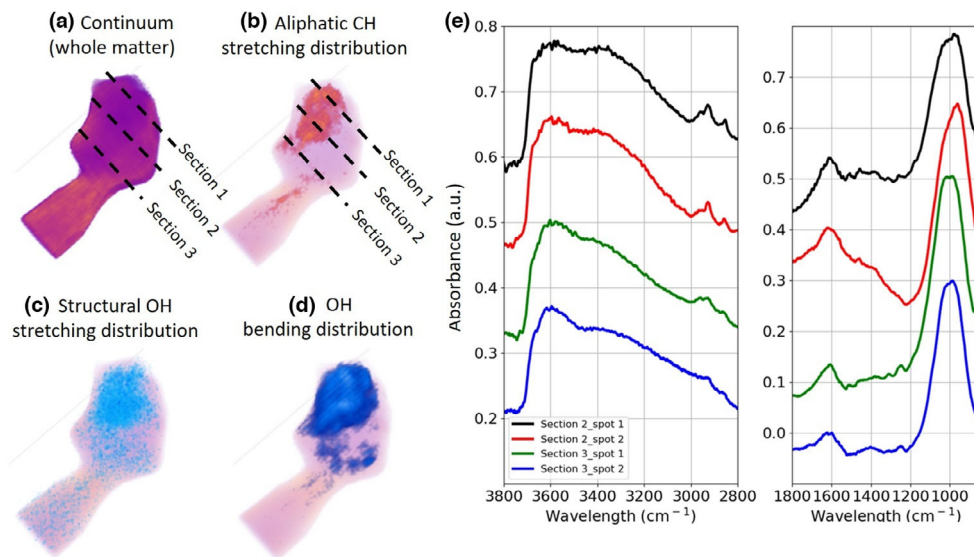


Fig. 6. a–d) 3D distribution of the whole matter (a), of the aliphatic CH stretching band (b), of the OH stretching bands (c), and bending band (d). On panels (a)–(d) are indicated the relative position of the three FIB sections taken from the AZ\_3 fragment. e) Spectra in transmission between 2600 and 3720  $\text{cm}^{-1}$  and between 850 and 1250  $\text{cm}^{-1}$  for different regions inside FIB sections 2 and 3.

between organic matter and surrounding silicates will be discussed for several fragments in the following section.

Moreover, we looked for structural heterogeneity of the organic matter inside this small fragment (AZ\_3 sections 1–3) both by studying the shape of the aliphatic stretching band with FT-IR and by analyzing the shape of Raman D and G bands. Focusing on the area rich in aliphatic CH bonds, we estimated the ratio  $\text{CH}_2/\text{CH}_3$  for spectra obtained by performing a spatial binning of nine pixels (close neighbors, a filter of 10% was applied to neglect pixels with low aliphatic CH band intensity). The fit was performed with the five Gaussians model described by Merouane et al. (2012). We obtained a value of  $1.2 \pm 0.2$  without any significant local difference within the sections. This value is of the same order of magnitude as previous values estimated on different CM (see for example Kebukawa et al., 2011). Raman spectroscopy was performed on the three sections from AZ\_3 to study the G and D bands (Busemann et al., 2007). These bands are sensitive to the structure and degree of order of the polyaromatic component in complex carbonaceous phases in meteorites (Quirico et al., 2014). The G band of AZ exhibits classical parameters for a CM chondrite: a maximum peak position around  $1595 \pm 5 \text{ cm}^{-1}$  and a full width half maximum (FWHM) around 90–100  $\text{cm}^{-1}$ . We found that the aromatic  $\text{C}=\text{C}$  was present in all the spectra measured inside the three sections. Still, we did not detect significant variations in intensity, in the position, or in the

FWHM of the G and D bands inside this small fragment (see Fig. 7c).

From SE images (Fig. 7a), we can estimate the porosity inside the three FIB sections. To cover a larger area of AZ and ensure a more representative perspective, we averaged the porosity estimated on the three sections, which gave a value of  $3.9 \pm 0.5\%$  inside the small fragment.

### Fragment Crushed Inside the Diamond Compression Cell

Finally, we present results obtained in transmission on the fragment AZ\_4 crushed inside the diamond compression cell. With this configuration, spectra show only upward absorption bands (absorbance y scale). The main feature is the silicate band at  $\sim 1000 \text{ cm}^{-1}$  (10  $\mu\text{m}$ ), that is typical of hydrated phyllosilicate minerals, the main component of the CM chondrite matrix (see Fig. 8 for different spectra inside AZ\_4). The shape and position of this peak are still consistent with the observation in reflection described above and correspond to a serpentine-rich sample. Another relevant absorption band is the large one due to  $\text{H}_2\text{O}$  stretching centered at  $3500 \text{ cm}^{-1}$  ( $\sim 2.9 \mu\text{m}$ ). The water bending mode (located at  $1640 \text{ cm}^{-1}$  [ $\sim 6.1 \mu\text{m}$ ]) is well separated from the rest of the  $1500 \text{ cm}^{-1}$  ( $\sim 6.7 \mu\text{m}$ ) multiplets which are due to organic components:  $\text{C}=\text{C}$  aromatic stretching and the  $\text{C}-\text{H}$  bending. Carbonates can also contribute to this band.

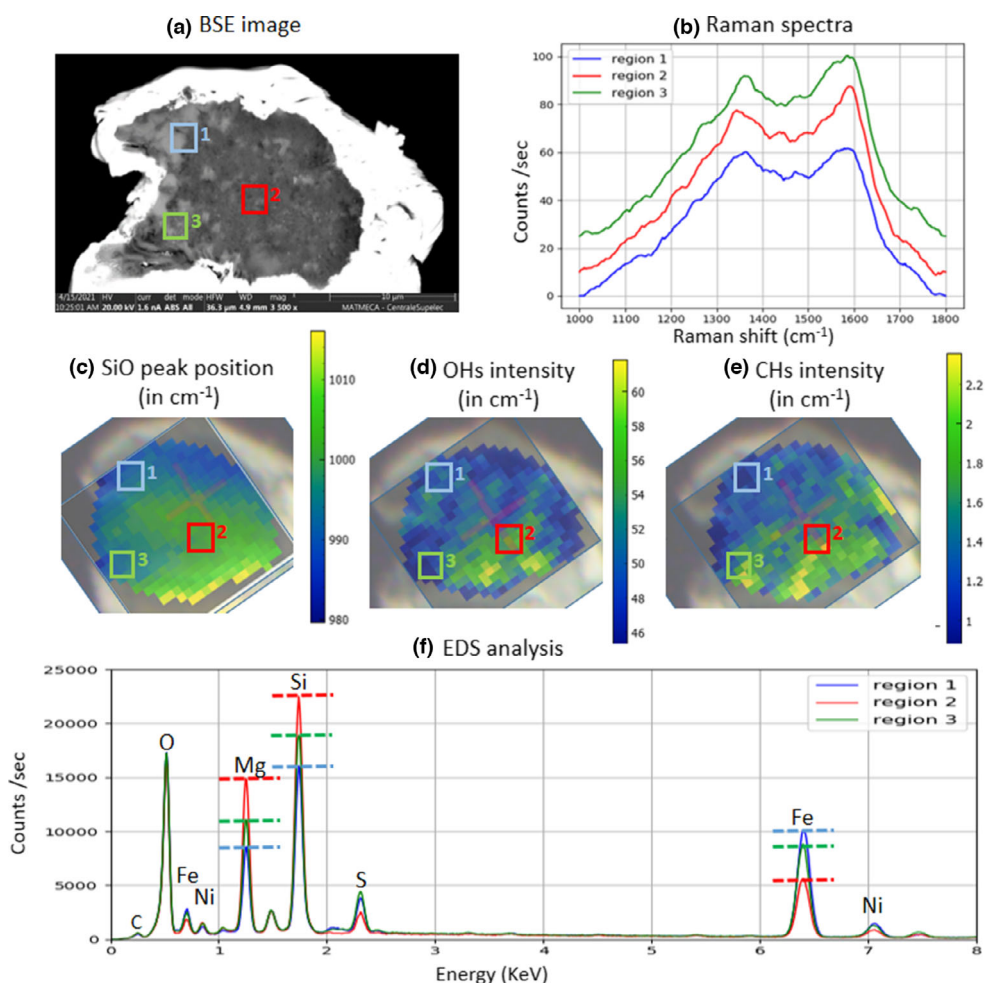


Fig. 7. a) Back scattering electron (BSE) image of section 3 and (b) Raman spectra for the three areas defined in panel (a). c–e) Spatial distribution inside section 2 obtained by FT-IR spectroscopy of the position of the maximum of the  $10\ \mu\text{m}$  band, of the intensity of the OH stretching band, and of the intensity of the aliphatic CH stretching band. f) Average EDS spectra in the three regions defined in panel (a).

We used five clusters (*k*-means clustering analysis) to analyze the spatial distribution of the different components in this part of the fragment. The result of this clustering is presented in Fig. 8. Clustering helps to rapidly identify regions with different spectral signatures. The carbonate-rich area stands out (cluster 1—orange spectra in Fig. 8b); we noticed a very strong band at  $1457\ \text{cm}^{-1}$  ( $\sim 6.9\ \mu\text{m}$ ) and its overtones at  $2510\ \text{cm}^{-1}$  ( $\sim 4.0\ \mu\text{m}$ ) and  $880\ \text{cm}^{-1}$  ( $\sim 11.4\ \mu\text{m}$ ) (Bruckman & Wriessnig, 2013). Complementary Raman analyses confirmed the presence of carbonates and allowed us to identify these as calcite. As in other CM chondrites (see De Leuw et al. [2010]; Dionnet et al. [2018]; Lee et al. [2014] for the case of the Paris meteorite), calcite spots are present as globules with a size of around  $30\text{--}40\ \mu\text{m}$ . Clusters 2–5 represent areas in the matrix with differences in intensity of the Si-O

and water bands. We observed a small shift in the position of the silicate band maxima between  $990\ \text{cm}^{-1}$  ( $\sim 10.1\ \mu\text{m}$ ; cluster 2) and  $1010\ \text{cm}^{-1}$  ( $\sim 9.9\ \mu\text{m}$ ; cluster 5). This gradual shift is correlated with water intensity variation from a weak water band (cluster 2) to a stronger one (cluster 5).

The aliphatic CH bands at  $2800\text{--}3000\ \text{cm}^{-1}$  ( $\sim 3.6\text{--}3.3\ \mu\text{m}$ ) also change in intensity between the different clusters and seem correlated with the strength of the water stretching bands, suggesting a link between the presence of aliphatic organic matter and hydration extent. Using the five Gaussians fit described in Merouane et al. (2012), we have estimated the  $\text{CH}_2/\text{CH}_3$  ratio for the different clusters. We found the same value  $1.3 \pm 0.3$  for all clusters. We observed a quantitative heterogeneity for the distribution of the organic matter but no structural difference at the scale of the fragment.

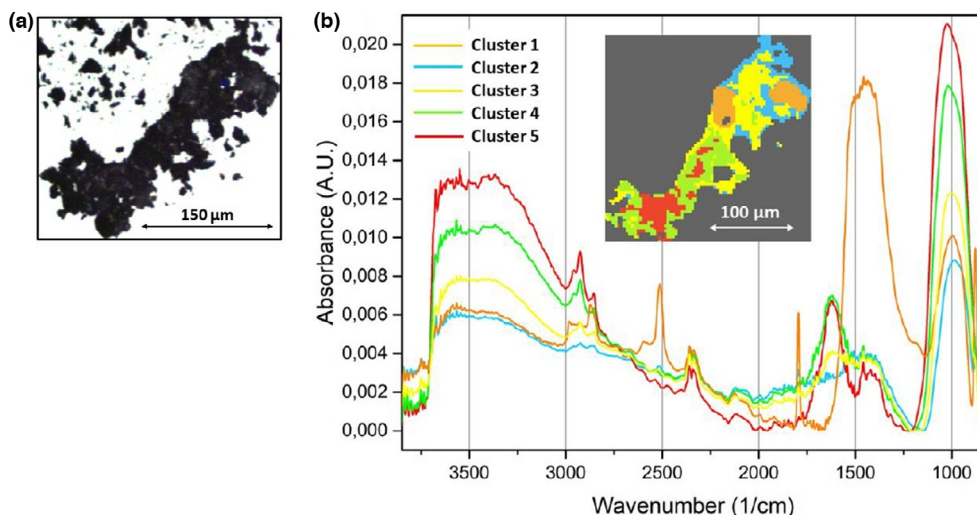


Fig. 8. a) Visible image of the first fragment after crushing. b) *k*-means clustering and average spectra for each cluster with associated colors.

Homogeneous aromatic components were also observed in the Raman spectra of this fragment as in fragment AZ\_3.

### Comparison of the Results Obtained on the Different Fragments

The study of different fragments at various scales and with different setups has revealed a complex structure. Focusing on the CM lithology, we have shown that it is composed of CAIs, Fe-Ni sulfides, elongated chondrules, and TCIs embedded in a fine-grained matrix, all visible in fragment AZ\_2 by XCT (see Fig. 2). IR spectroscopy (on fragments AZ\_1, AZ\_3, and AZ\_4) revealed that the matrix is mainly composed of serpentine with an internal variation of Mg/Fe ratio, visible in the shift of the 10  $\mu\text{m}$  band. This heterogeneity is spatially correlated with various degrees of hydration: the regions enriched in Mg (with spectra showing a SiO band with a maximum around  $1010\text{ cm}^{-1}$  [ $\sim 9.9\text{ }\mu\text{m}$ ]) correspond to the most hydrated areas. The correlation between an increase in Mg and hydration is a trend already observed in CC meteorites by Tomeoka et al. (1989), Browning et al. (1996), and Hanna et al. (2020). The aliphatic CH band intensity is also correlated with the strength of the water stretching bands. We did not detect any structural heterogeneity of the aliphatic matter inside single fragments or, at a larger scale, between two fragments originating from different locations inside the matrix of the CM-like lithology (similar  $\text{CH}_2/\text{CH}_3$  ratio of  $1.3 \pm 0.3$  for fragments AZ\_3 and AZ\_4). Thus we observed a quantitative heterogeneity for the distribution of the

organic matter but no structural differences. A study of Raman spectra also shows that the distribution of the aromatic C = C is quite homogeneous at the scale of micrometric fragments. The distribution of polyaromatic carbon compounds appears unrelated to the distribution of aliphatics. In addition, we have estimated a porosity around 4.5 vol% in fragment AZ\_2, mainly due to elongated pores/fractures. Within error bars, the value of porosity estimated on AZ\_3 sections is consistent with the value estimated for the larger fragment AZ\_2.

## DISCUSSION

### Matrix Properties and Comparison with Other CMs

To compare the average composition detected by FT-IR, we have plotted the reflectance spectra of AZ and other CM chondrites. The comparison data set was collected during the past few years using the same experimental setup at SOLEIL, and most of the samples were prepared at Tohoku University in the framework of a rehearsal campaign for Hayabusa2, although some of the samples were prepared previously as powders compressed into pellets (see Lantz et al., 2017). In Fig. 9a, we show the average reflectance spectra of our different meteorite samples obtained at large scale (mm-sized spot), focusing on the structure of the 10  $\mu\text{m}$  band ( $1000\text{ cm}^{-1}$ ). The spectra were scaled to unity at the main peak position, in order to stress how the position and profile of the 10  $\mu\text{m}$  band change moving from the meteorites with a matrix dominated by phyllosilicates (left panel, main peak position typically above

1000  $\text{cm}^{-1}$ ), to primitive CM2 meteorites such as Paris or Murchison showing the presence of partly amorphous hydrated silicates in the matrix as well as abundant anhydrous phases in chondrules (central panel), down to meteorites dominated by anhydrous phases both in the matrix and chondrules (right panel, main peak position below 1000  $\text{cm}^{-1}$  [10  $\mu\text{m}$ ], usually determined by olivines). In other words, the average large-scale spectra of the considered meteorites carry information about their matrix mineralogy and relative phase abundances and its relative abundance with respect to other phases such as those in chondrules or inclusions (Cloutis et al., 2011; Noun et al., 2019; Potin et al., 2020).

In order to build a convenient graph that would allow a quick comparison among the analyzed samples, we report the peak position of the main Si-O band with respect to the minimum of the first derivative after the 10  $\mu\text{m}$  band. This last parameter corresponds to an inflection point of the spectrum and to the point with a minimum slope on the left part of the SiO band (e.g., between 1000 and 1100  $\text{cm}^{-1}$  for AZ). These parameters are diagnostic of the composition and structure of the main minerals of the meteorites. In Fig. 9b we can clearly separate the region of meteorites with a phyllosilicate-rich matrix (e.g., Orgueil) on the right, the most primitive meteorites (e.g., CM2 Paris) at the center of the graph, and the most heated meteorites (e.g., Allende) whose matrix is rich in anhydrous phases. This kind of representation could be useful to estimate the approximate degree of aqueous alteration and the relative amount of heating undergone by a meteorite based on the spectral parameters (Beck et al., 2018; Cloutis et al., 2011; Hanna et al., 2020). AZ is between the region with phyllosilicate-rich matrix and the region corresponding to the primitive meteorites. This confirms a moderate degree of aqueous alteration as concluded by previous research (Davidson et al., 2020). Moreover, the presence of more than one distinct lithology confirms its description as a brecciated meteorite given in the Meteoritical Bulletin.

The spectrum of Bennu obtained with OTEs (Hamilton et al., 2021) was added in Fig. 9 for comparison; its characteristics are close to the one of CM primitive meteorites as predicted in the literature. In 2021, the James Webb Space Telescope was launched with the instrument MIRI onboard. This instrument can focus on the 10  $\mu\text{m}$  band of an asteroid's spectrum with a spectral resolving power  $R \sim 3000$  (Wells et al., 2015), which is large enough to distinguish spectra from different areas defined in Fig. 9b. However, the signal-to-noise ratio has to be really good to precisely extract the 10  $\mu\text{m}$  band's parameters and could be the limiting factor.

### Aqueous Alteration Inside AZ

From our data, we can estimate with two independent methods the petrologic subtype of the CM-like lithology inside AZ and discuss the degree of hydration experienced by our fragments. The first method uses the FT-IR data in reflectance. Hanna et al. (2020) defined a mathematical expression to correlate the degree of aqueous alteration and Si-O stretching spectral features in CMs. They showed that a high degree of alteration is directly proportional to a decrease of the difference, in wave numbers, between the Christiansen feature and the Si-O stretching band center. Since an increase in aqueous alteration extent among CMs corresponds to a lower petrologic subtype, by assessing the position of these two spectral features, a further classification and comparison of the meteorites can be achieved. The mathematical correlation is  $\text{petrologic subtype} = (y + 105.2)/122.2$ , where  $y$  represents the difference in wave numbers between the Christiansen feature and Si-O stretching band.

We analyzed the reflectance spectra shown in Fig. 10 in a similar way. Reflectance spectra were treated by extracting relevant spectral parameters. Similar to the results found in Hanna et al. (2020), the difference between the Christiansen feature and the maximum of the Si-O peak position seems to be a reliable parameter for predicting the subpetrologic type of CM chondrite samples ( $r = 0.82$ ). In our case, we found the relation with the petrologic type  $= (y + 256.7)/184.4$ , where  $y$  represents the difference in wave numbers between the Christiansen feature and Si-O. The trend observed in Hanna et al. (2020) was confirmed in this study by using the same method on a different set of samples (which can explain the variation between the coefficient of linear regression). Using the interpolation obtained based on the difference between the Christiansen feature and the maximum of the Si-O peak position, we found a petrologic type between 2.4 and 2.5 using our data in reflectance (see Fig. 10).

The second method is based on the quantification of TCIs. The quantity of TCIs estimated inside our large fragment is around  $26 \pm 2$  vol%. Rubin et al. (2007) predicted between 20% and 40% of TCIs for a CM depending on aqueous alteration. They proposed a relationship between the petrologic type of carbonaceous chondrites to the percent of TCIs present in the fragment. The 26 vol% estimated by XCT analyses of the CM-like lithology corresponds to a petrographic type of  $2.4 \pm 0.2$ . The two methods (obtained from XCT and FT-IR) give compatible values for the extent of aqueous alteration. Furthermore, they are largely in agreement with previous literature

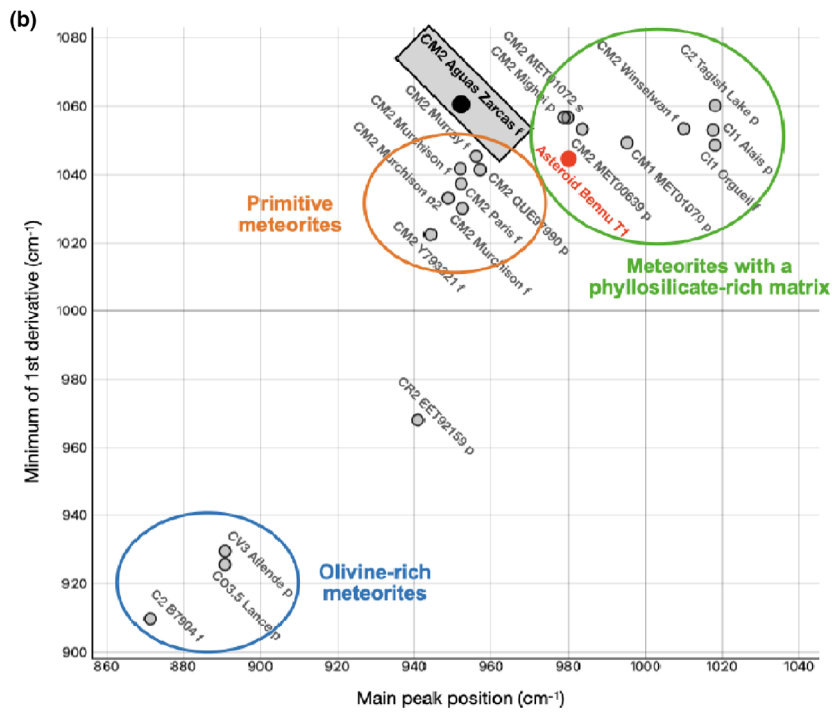
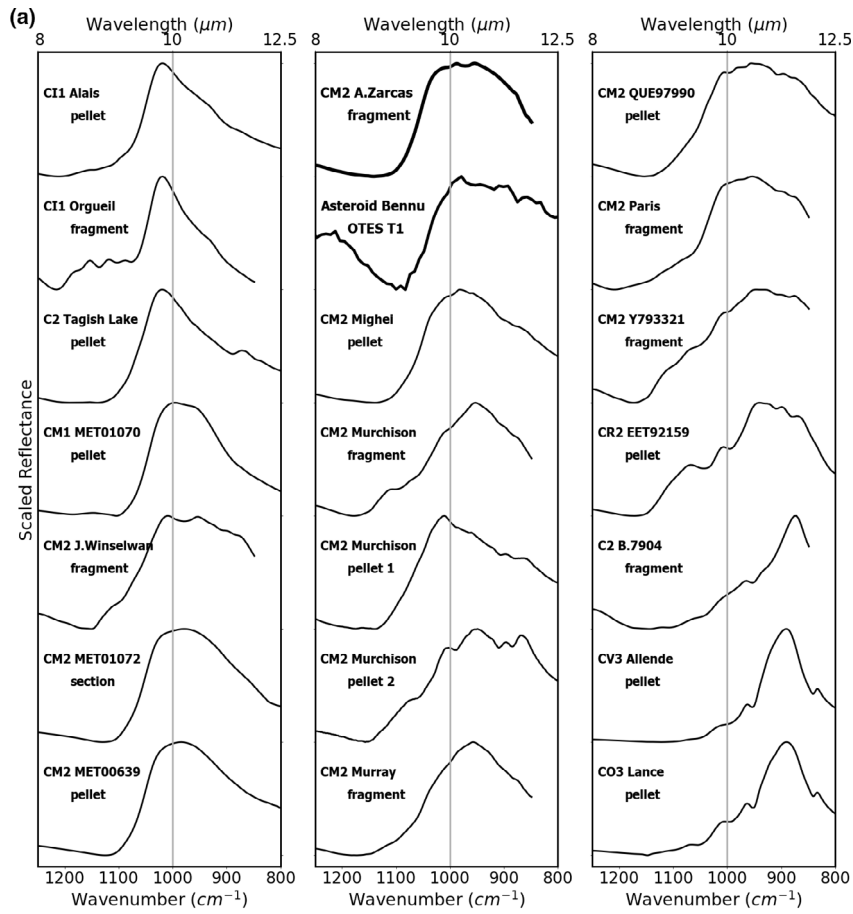


Fig. 9. a) The average large-scale (mm-sized spot) MIR reflectance spectra of the meteorites selected in this study. The spectral range is restricted to the values corresponding to the surface scattering regime (Christiansen features and main reststrahlen bands), with particular emphasis on the Si-O stretching bands. All the spectra were scaled to unity at the position of their main Si-O stretching band, but without performing a continuum removal. Pellet refers to compressed meteorite powders; fragments refer to the surface of 3D samples. The spectra of Tagish Lake, Mighei, Alais, Allende, and Lancé come from Lantz et al. (2017). The spectra of Murchison pellets come from Lantz et al. (2015). The spectrum of Paris comes from Noun et al. (2019). The spectrum of Bennu comes from Hamilton et al. (2021). b) The minimum of the first derivative versus the peak position of the main Si-O band, for the average large-scale spectra of the considered meteorites.

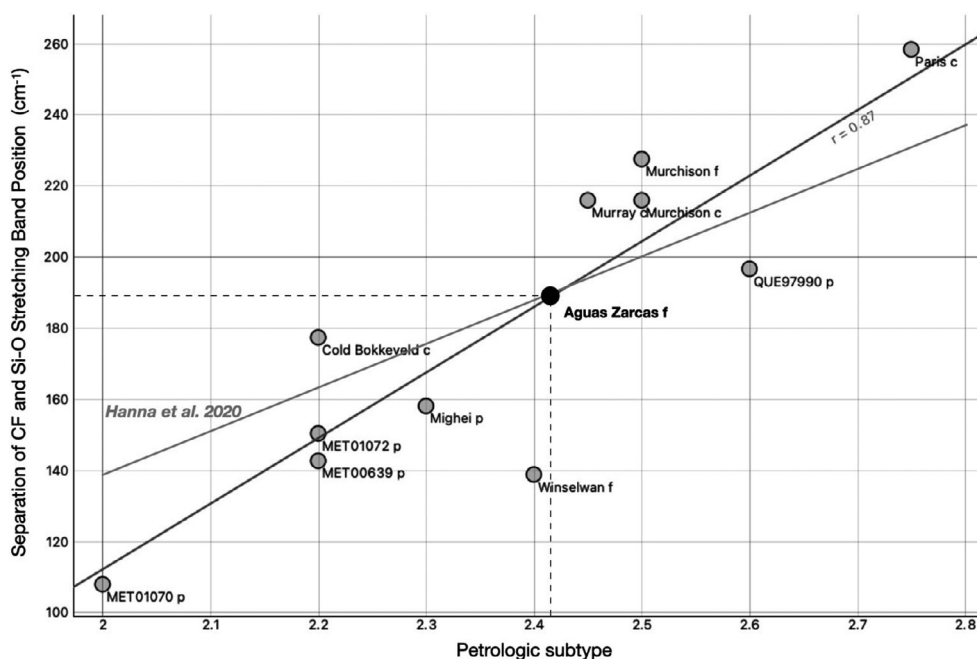


Fig. 10. Difference between the Christiansen feature and the position of the maximum of the main Si-O peak obtained on reflectance spectral parameters according to the petrological type. The dark line represents the fit obtained with our data and the gray line represents the fit obtained by Hanna et al. (2020). This last fit has been obtained by a similar method but with a different set of meteorites.

assessments: three clasts with petrological type 2.6 (for the two first clasts) and 2.8 (for the third clast) were observed in the CM-like lithology by Kerrouach et al. (2021), while Davidson et al. (2020) described a fragment with a petrological subtype between 2.2 and 2.4.

### Organic Matter Description and Heterogeneity in the Mineral Context

In this section, we focus on the relation between the organic and minerals phases. Figure 11 shows the distribution of three parameters (the position of the maximum of the silicate band, the intensity of aliphatic organic matter, and the degree of hydration) as a function of each other for each pixel of the two fragments studied in transmission, i.e., the fragment

crushed inside a diamond compression cell (AZ\_4) and the sections from the 3D small fragment (AZ\_3). Our data reveal a positive correlation between aliphatic organic matter abundance and hydration extent ( $H_2O$  abundance), and by inference the degree of aqueous alteration. In both fragments, pixels enriched in organic matter have correspondingly stronger OH signatures. The same pixels also show a maximum of the silicate band between  $990$  and  $1010\text{ cm}^{-1}$  ( $\sim 10.1$  to  $9.9\text{ }\mu\text{m}$ ), which corresponds to silicate enriched in magnesium compared to the rest of the fragment. The two fragments have different sizes. Thus, the heterogeneity in two areas separated by more than  $150\text{ }\mu\text{m}$  (in the case of the crushed fragment) is also observable over a comparable range inside a single fragment, between two locations separated by less than  $20\text{ }\mu\text{m}$ .



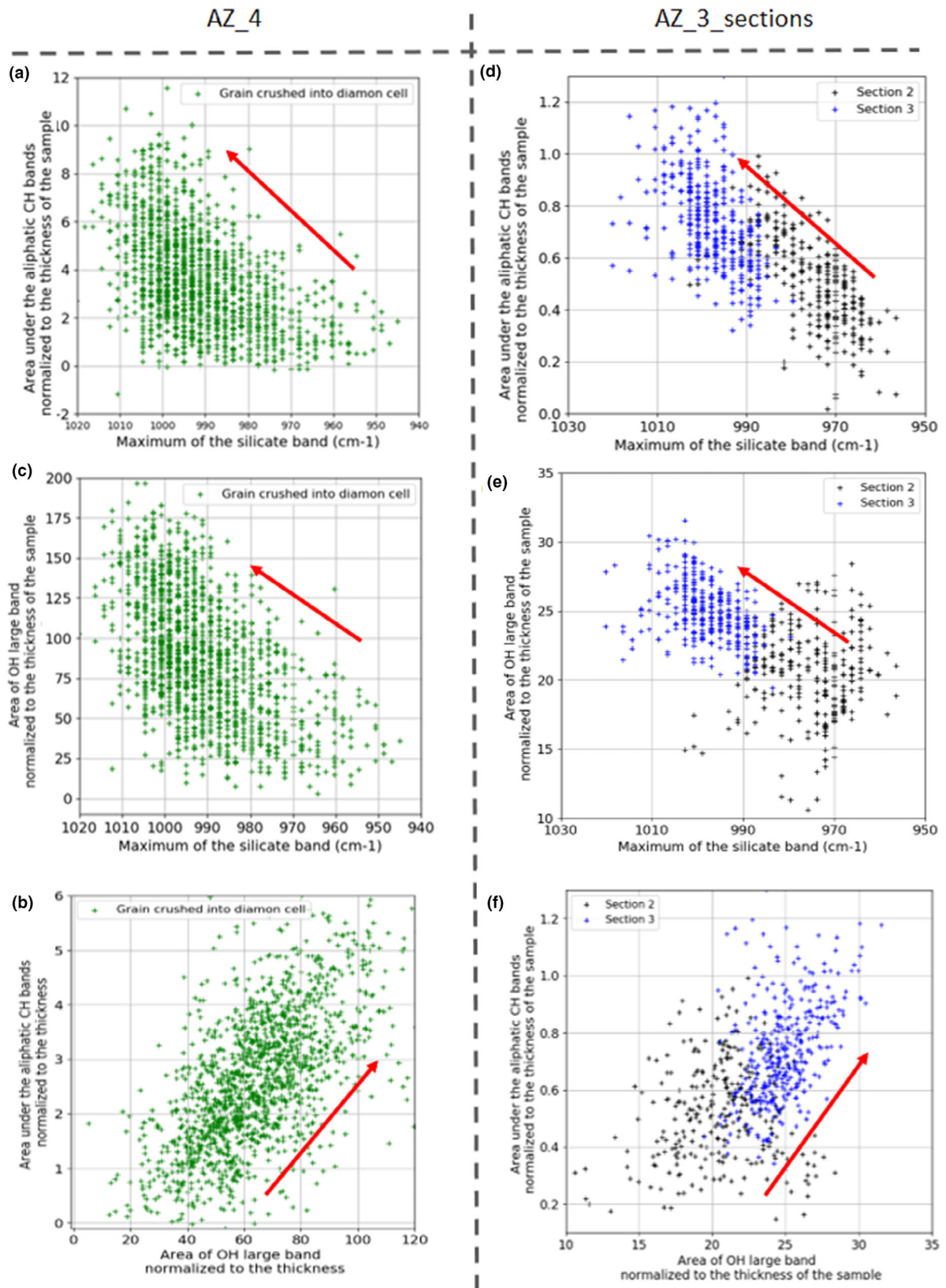


Fig. 11. Correlation diagrams for the fragment AZ\_4 crushed into the diamond compression cell (panels [a]–[c]) and for the sections AZ\_3\_sections (panels [d]–[f]). a and d) Position of the silicate band maxima versus intensity of the aliphatic organic matter. b and e) Position of the silicate band maxima versus the degree of hydration. c and f) Intensity of the aliphatic organic matter versus the degree of hydration. The intensity of the aliphatic organic matter and the degree of hydration are estimated by calculating the area, respectively, under the CH aliphatic features (integration after a baseline correction between 2826 and 3007  $\text{cm}^{-1}$ ) and the OH stretching feature (after a baseline correction between 3015 and 3631  $\text{cm}^{-1}$ ). A normalization by the thickness of the sample (i.e., 3  $\mu\text{m}$ ) is moreover performed to obtain the degree of hydration.

Organic matter is not homogeneously distributed inside the studied CM chondrite. We detected hotspots of organic aliphatic matter that are correlated with more hydrated regions within the fragment (those enriched in Mg-bearing silicates). This suggests that aqueous alteration in the AZ parent body played a major role in the evolution of the organic matter in agreement with previous studies on other CM chondrites, such as Le Guillou et al. (2014), Vinogradoff et al. (2017), and Noun et al. (2019). On the contrary, the aromatic compounds detected using Raman spectroscopy appear to be homogeneously distributed at the  $\mu\text{m}$ -scale and unaffected by variations in the extent of aqueous alteration. Variations in the  $\text{CH}_2/\text{CH}_3$  ratios in AZ at the micrometer scale were not detected. This implies no changes in the aliphatic organic matter branching degree in the fragment. Vinogradoff et al. (2017) emphasized a correlation between water alteration and the heterogeneity of the organic matter. Dionnet et al. (2018) demonstrated a heterogeneous  $\text{CH}_2/\text{CH}_3$  ratio inside a single fragment of the Paris meteorite. The petrologic subtype of AZ is lower than that of Paris (reflecting more advanced alteration in the AZ fragment) and this might explain the homogeneity of the aliphatics observed here (Isa et al., 2021). An extensive aqueous alteration process may cause a further homogenization of organic matter and it can be the reason why no variation of the  $\text{CH}_2/\text{CH}_3$  ratios in different hydration zones has been observed in this work. Concerning the aromatic signature, neither variation of intensity nor various band profiles were observed in our fragment (we observed the same D and G bands everywhere inside our fragments). The G band exhibits its main peak position around  $1590 \pm 5 \text{ cm}^{-1}$  and the FWHM is between 90 and  $100 \text{ cm}^{-1}$ , which is typical for CM chondrites (Busemann et al., 2007). The absence of modification of the Raman signature in the more altered regions suggests that the aqueous alteration leaves the polyaromatic compounds unaffected. At the same time, a higher concentration of aliphatic organic compounds in the same regions suggests that aqueous alteration may have been responsible for the generation of new aliphatic molecules.

### Scale of the Porosity

We performed two independent estimates of porosity applied at different scales and using distinct analytical approaches. First, the XCT data gave a value of  $4.5 \text{ vol}\% \pm 0.5$  by counting voxels with a low LAC. The LAC is not sensitive to low-Z materials (Z being the average atomic number); thus, some voxels, considered as empty voxels by XCT, may contain low-Z material, such as organic matter. Matrajt et al. (2012) as well as De Gregorio et al. (2013), Changela et al. (2018), Le Guillou et al. (2014), Floss et al. (2014), and Nakamura-Messenger et al. (2006) have observed different types of organic matter in extraterrestrial material using transmission electron microscopy. They observed organic globules with a size from 30 to 500 nm. Similar features may be contained inside the pore distribution observed in our fragments. The largest ones have sizes similar to the voxel in our study. The second value of porosity, estimated using image analysis of the SEM images of the FIB sections of the smallest fragment of AZ, can help resolve this issue, as in the case of SE images, black pixels could only be voids. Moreover, the resolution is better with SE images and we should be able to see pores as small as  $0.1 \mu\text{m}$  (versus a resolution of  $1 \mu\text{m}$  for XCT analyses). This method gives us a porosity of  $3.9 \pm 0.5 \text{ vol}\%$ . The fact that the second estimation gives a slightly lower value confirms that “pores” voxels counted as pores by XCT are mainly empty and not full of low-density matter. There is only a small difference between the two values, meaning that the majority of pores described in this paper are bigger than  $0.1 \mu\text{m}$ .

However, the values of porosity found here are small compared to expected values for CM chondrites as estimated in Consolmagno et al. (2008). Various values of porosity can be found for CM fragments depending on the method of measurement and the size of the fragment studied. Consolmagno et al. (2008) found values around 20–25 vol% for porosity in CM chondrites by using pycnometry while the point-counting method finds 3–4 vol% porosity (Corrigan et al., 1997). As explained in Consolmagno et al. (2008), this could be due to the scale of porosity: “The

difference between point-counting and He/bead porosity measurements most likely indicate that the porosity in carbonaceous chondrites is found on a scale either too large or too small to be seen easily in thin section.” This means that in the measurement of small fragment volumes we necessarily miss porosity whose scales are larger than the size of the fragment or smaller than  $0.1\ \mu\text{m}$ .

With our measurements, we are sensitive only to the microporosity. The magnitude of our measurement is consistent with values obtained by image treatment (Corrigan et al., 1997; Hezel et al., 2013). According to Friedrich et al. (2017), XCT measurement is comparable to ideal gas pycnometry for ordinary chondrites when measuring with a resolution below  $2.6\ \mu\text{m}$ . The resolution in our data is much better than the one used by Friedrich et al. (2017), but working with carbonaceous chondrites, we notice that the difference is important. We also observed anisotropy in the distribution of pores, with different values for pores inside the matrix versus pores inside the chondrules. The anisotropy is more significant for pores inside the matrix. Pores are primarily due to the presence of large-scale cracks and most likely originate due to shock effects such as thermal shocks and impacts. Smaller pores present inside the “compact” matrix should be present as nanometric pores but are not visible at our scale. This observation fits well with the description of the porosity at fine scales inside the primitive carbonaceous chondrite Paris observed by Zanetta et al. (2021). In addition, the difference between our values and the 25 vol% measured by Consolmagno et al. (2008) is probably due to pores at millimetric scales, not visible in our fragments because of their sizes. Such big pores would have weakened the fragments too much and they would have broken.

To sum up, pore size distribution is a continuum in carbonaceous chondrites between the nanoscale, mainly contained in the matrix of amorphous silicates (Zanetta et al., 2021), the micron-scale features seen in XCT and to larger mm-to-cm-scale. The different size regimes observed during studies is inherent in the techniques used but various papers also suggest that these three scales could be representative of different processes that happened at different times in the history of carbonaceous chondrite: Nanoscale porosity present in fine-grained rims could be characteristic of the nebula processes before matrix accretion (Zanetta et al., 2021) or could be residual porosity of the accretional phases, such as voids left after the melting of water-ice (Matsumoto et al., 2019; Trigo-Rodriguez et al., 2006), while bigger pores (micron to cm scales) could be the result of secondary processes such as circulation of fluids, shock, thermal fracture, or dehydration (DeCarli

et al., 2001). In addition to these scales, a population of much larger voids (occasionally termed macroporosity) are expected to exist on second-generation rubble-pile asteroids (such as Ryugu and Bennu). These large meter-scale voids are necessary to account for the anomalously low densities of some asteroids (Britt et al., 2002). For instance, Cambioni et al. (2021) have estimated that the porosity of the meter-sized boulders on the surface of Bennu can reach up to 50%–60%. At this large scale, pores are mainly due to impacts (Avdellidou et al., 2020) and thermal fatigue (Delbo et al., 2014).

### **Petrofabrics and Porosity of AZ Chondrules: Origin and Evolution**

The size of the chondrules is in agreement with literature data: the mean average size of chondrules is around  $300\ \mu\text{m}$  for CM chondrites (Weisberg et al., 2006) but Kouvatsis and Cartwright (2020) observed chondrules up to  $1500\ \mu\text{m}$  in a chondrule-rich CM lithology of AZ.

Chondrules also have elongated shapes. The size of the chondrules is in agreement with literature data: the mean average size of chondrules is around  $300\ \mu\text{m}$  for CM chondrites (Weisberg et al., 2006). The elongate shape of chondrules was also reported by Yang et al. (2021) inside a compact lithology present in AZ and could be due to hypervelocity impacts. Indeed, they have proposed a formation model for AZ involving a “series of ejection and reaccretion of sub-cm-sized fragments produced by ejection events” to explain the presence of various lithologies including those that show evidence of strong impacts.

We measured a porosity value of  $6.3 \pm 1\ \text{vol}\%$ . Lewis et al. (2018) and Macke et al. (2011) performed similar measurements with XCT and both concluded that porosity is significantly higher in the matrix than in the chondrules. Quantitative measurements of the porosity inside chondrules has been performed in only a few papers and they predict very low values: around 1–2 vol% (Lewis et al., 2018) in L4 ordinary meteorites and 0.1–0.6% of porosity in the chondrules of Allende (Ebel & Rivers, 2007). Regions of high porosity are either close to fractures inside the fragment, which could have facilitated water passage, in or around chondrules. However, both meteorites studied in these papers are metamorphosed with clear evidence of growth of new minerals that will likely reduce porosity. On the contrary, Hanowski and Brearley (2001) characterized 35 chondrules inside a single CM and have shown that the effect of aqueous alteration is very different according to the type of chondrules: the dissolution of primary phases could explain high porosity especially in the case of

clinoenstatite-rich chondrules. Measurements for porosity inside chondrules in CM chondrites are currently absent and our study brings a first order of magnitude value for chondrule porosity in CM chondrites.

In the following discussion, we outline how chondrule porosity may be expected to evolve over the geological history of a chondrite parent body:

(i) Due to heating effects during chondrule formation: Inside unaltered chondrules, since they have igneous origins, any internal void space is most likely to be irregular interstitial space between crystals and is formed by volume contraction. The molten droplet will take less volume than the cooled solid and cooling from the outside inwards will create void space, probably near the center as observed in I-type cosmic spherules described by Feng et al. (2005) and Genge et al. (2017). The location of the voids inside chondrules will discriminate against this hypothesis. In our case, the voids are equally spread inside the chondrules, thus the heating effect cannot explain the high value of porosity found in chondrules inside our sample.

(ii) Accretional porosity present inside fine-grained rims: A small part of the porosity could be present in the edge of the chondrules in their inner fine-grained rim. Trigo-Rodriguez et al. (2006) argued that fine-grained rims around some chondrules in CM meteorites preserve their original accretionary porosity. By contrast, much of the remaining fine-grained matrix is instead affected by impact-induced compaction and therefore exhibits lower porosity values. The matrix could have been compacted with strain accommodated by primarily deformation of the matrix, leaving the chondrules unaltered (Bland et al., 2014, Davison et al., 2016; Forman et al., 2017). Zanetta et al. (2021) have also observed a higher porosity at the edge of chondrules in Paris fine-grained rims. In our case, a manual check confirms the presence of slightly more porous regions around the chondrules, but it does not explain the high porosity detected for chondrules in this study. Chondrule porosity is unlikely to be accretional residual porosity.

(iii) Aqueous alteration progressively replaces the primary accretionary phases in carbonaceous chondrites with secondary minerals. In chondrules, the glass and Fe-Ni-metal are highly susceptible to fluids and alter first while more resistant anhydrous silicates (olivine and pyroxene) alter later. Secondary mineralization processes typically operate by direct replacement, producing pseudomorphic forms that preserve the habit and texture of their former primary phases (Hanowski & Brearley,

2001; Velbel et al., 2012, 2015). This explains why pseudomorphic chondrule outlines are observed in heavily altered CM2s and CM1 chondrites (Grady et al., 1987; Zolensky et al., 1997). However, not all primary minerals experience isovolumetric replacement. For example, Lee and Lindgren (2016) documented the presence of void spaces (pores) in partially altered forsterite and clinoenstatite grains. These void spaces are crystallographically controlled, being oriented parallel to the (010) and (001) axes in forsterite and the (001) axis in clinoenstatite. They are interpreted as having formed by congruent dissolution. As alteration advanced, these voids were subsequently infilled by a later generation of polyhedral serpentine. Dissolution during aqueous alteration is therefore a potential explanation for the origin of chondrule voids. However, the chondrules identified in this study contain both chondrule metal and bright Fe-rich anhydrous silicates. The retention of these fluid-susceptible phases implies chondrules have suffered a low degree of alteration. Dissolution could be only partially responsible for the high chondrule porosity values that we have observed.

(iv) Due to shocks: Impact compaction and brittle failure will create secondary porosity in the form of fractures. The fractures will be linear and branched so that they can be easily discriminated. We have estimated the value of anisotropy of voids inside chondrules to discriminate this hypothesis and it gives a value of 6.25, meaning elongated pores inside chondrules. The chondrules are elongated and this seems to corroborate the shock scenario (cf. Hanna et al., 2015). Lindgren et al. (2015) have also studied the effect of flattening of chondrules due to shock inside CM chondrites, and argued that chondrule flattening occurred after alteration, and thus changed the shape of pores produced by aqueous alteration. It makes the effect of alteration hard to distinguish from the effect of shock when speaking of the shape of pores inside chondrules. It is likely that the elongated void pattern visible in our sample is the result of a moderate aqueous alteration followed by a shock episode.

We conclude that porosity inside chondrules examined in this paper is then primarily due to shocks and, to a lesser extent, to dissolution during aqueous alteration. In a CM 2.5 chondrite, aqueous alteration could dissolve anhydrous silicates (Velbel et al., 2015). However, more data on other CM chondrite chondrule porosity would be very useful to better understand the phenomena which produce porous chondrules.

## CONCLUSION

This study focused on the CM chondrite AZ, investigated with both FT-IR spectroscopy and XCT analyses. Analyses were performed at different scales to better understand its complex history and specifically to clarify the following points:

(a) We obtained a global description of our different fragments. We observed two lithologies inside our biggest fragment AZ\_1: one similar to the C1 lithology described by Kerraouch et al. (2021), and a CM-like lithology. Comparing this last one with other CM carbonaceous chondrites, we can describe AZ's CM lithology as an intermediate between carbonaceous chondrites with phyllosilicate-rich matrix and the least altered carbonaceous chondrites.

(b) Concerning the extent of aqueous alteration, both techniques used in this paper have converged to classify our CM-like fragment as a CM2.5. Moreover, we have confirmed the conclusion of Hanna et al. (2020): the difference between the maximum of the Si-O band and the Christiansen feature extracted from measurement in reflection is a suitable parameter to predict the petrological subtype of a new CM chondrite.

(c) In addition, a study of porosity, pore distribution, and pore shape allowed us to evaluate the extent to which secondary processes have affected AZ: in addition to a moderate degree of aqueous alteration, this meteorite has also undergone shock processing.

(d) Concerning the organic component, we found spatial heterogeneity in abundance: a higher concentration of aliphatic organic compounds correlated with more hydrated regions enriched in Mg-bearing silicates. Our results revealed a positive correlation between more advanced aqueous alteration and higher aliphatic matter abundances. This suggests that aqueous alteration may have been responsible for the generation of new (biologically important) aliphatic molecules while apparently leaving larger polyaromatic compounds unaffected.

This paper was also an opportunity to discuss new tools useful to describe the diversity of carbonaceous chondrites. Spectral parameters of FT-IR measurement in reflection were extracted and placed in a diagram that allows a quick comparison of any new sample measured in the same condition with other carbonaceous chondrites. The projection of hyperspectral imaging measurements in reflectance onto a 3D volume has been performed using the 3D model obtained with a reconstruction based on SEM images, which is also a novel method at the scale of the individual grain. Such nondestructive measurement could be rapidly performed at the surface of any new sample thanks to

IR-SI and will be particularly useful in the near future, with the return of precious extraterrestrial material by sample return missions. It will be helpful to reveal trends that could be sought at a scale in remote sensing data sets. It will help to build a bridge between the remote sensing observations of asteroid surfaces and the chemical and physical processes operating between the milliscale and the nanoscale characterized in the laboratory.

Estimations of porosity for the whole fragment and inside the chondrules were performed and showed that (i) porosity measurements on meteorites should always come with a caveat of the size range over which they are valid; (ii) different ranges of pore sizes could be representative of different stages of the sample's history; and (iii) chondrules can also contain pores, especially those created by secondary processes on the parent bodies, as in our case. More 3D studies focusing on the size distribution and spatial distribution of pores inside CMs are needed to understand the complex structural properties of primitive bodies.

*Acknowledgments*—Z. Dionnet was supported by a CNES postdoctoral allocation and by the Italian Space Agency within the ASI-INAF agreements I/032/05/0 and I/024/12/0. C. Avdellidou acknowledges funding support from the National Research Agency (ANR), project ORIGINS (ANR-18-CE31-0014). We acknowledge SOLEIL for provision of synchrotron radiation on ANATOMIX facilities through the proposal 20191248. ANATOMIX is an Equipment of Excellence (EQUIPEX) funded by the Investments for the Future program of the French National Research Agency (ANR), project NanoimagesX, grant no. ANR-11-EQPX-0031. The microspectroscopy measurements were supported by grants from Region Ile-de-France (DIM-ACAV) and SOLEIL. FIB sectioning and SEM images were acquired from a dual-beam microscope which is part of the MATMECA platform, supported by the “Investissement d’avenir” program (n°ANR-10-EQPX-37). This work was also supported by the Centre National d’Etudes Spatiales (CNES-France, Hayabusa2 mission). We thank J. Aleon, T. Hiroi, E. Quirico, P. Beck, and M. Zolensky for providing us with meteorite samples, and V.E. Hamilton and A. Brearley for their constructive comments on the manuscript during review.

*Data Availability Statement*—The data that support the findings of this study are available from the corresponding author upon reasonable request.

*Editorial Handling*—Dr. Daniel Glavin

## REFERENCES

- Aléon-Toppani, A., Brunetto, R., Aléon, J., Dionnet, Z., Levy, D., Troadec, D., Rubino, S., Brisset, F., Borondics, F., and King, A. 2021. A Preparation Sequence for Multi-Analysis of  $\mu\text{m}$ -Sized Extraterrestrial and Geological Samples. *Meteoritics & Planetary Science* 56: 1151–72.
- Avdellidou, C., Di Donna, A., Schultz, C., Harthong, B., Price, M. C., Peyroux, R., Britt, D., Cole, D., and Delbo, M. 2020. Very Weak Carbonaceous Asteroid Simulants I: Mechanical Properties and Response to Hypervelocity Impacts. *Icarus* 341: 113648.
- Bates, H. C., King, A. J., Donaldson Hanna, K. L., Bowles, N. E., and Russell, S. S. 2020. Linking Mineralogy and Spectroscopy of Highly Aqueously Altered CM and CI Carbonaceous Chondrites in Preparation for Primitive Asteroid Sample Return. *Meteoritics & Planetary Science* 55: 77–101.
- Beck, P., Garenne, A., Quirico, E., Bonal, L., Montes-Hernandez, G., Moynier, F., and Schmitt, B. 2014. Transmission Infrared Spectra (2–25  $\mu\text{m}$ ) of Carbonaceous Chondrites (CI, CM, CV–CK, CR, C2 Ungrouped): Mineralogy, Water, and Asteroidal Processes. *Icarus* 229: 263–77.
- Beck, P., Maturilli, A., Garenne, A., Vernazza, P., Helbert, J., Quirico, E., and Schmitt, B. 2018. What Is Controlling the Reflectance Spectra (0.35–150  $\mu\text{m}$ ) of Hydrated (and Dehydrated) Carbonaceous Chondrites? *Icarus* 313: 124–38.
- Bland, P. A., Collins, G. S., Davison, T. M., Abreu, N. M., Ciesla, F. J., Muxworthy, A. R., and Moore, J. 2014. Pressure-Temperature Evolution of Primordial Solar System Solids During Impact-Induced Compaction. *Nature Communications* 5: 1–13.
- Brearley, A. J. 2013. Nebular vs Parent Body Processing of Chondritic Meteorites. In *Meteorites, Comets and Planets*, 2nd ed., edited by A. M. Davis, 309–34. Cambridge: Elsevier.
- Brearley, A. J., and Jones, R. H. 1998. Chondritic Meteorites. In *Planetary Materials, Reviews in Mineralogy*, edited by J. J. Papike, vol. 36, 3-001–3-398. Chantilly, Virginia: Mineralogical Society of America.
- Britt, D. T., Yeomans, D., Housen, K., and Consolmagno, G. 2002. Asteroid Density, Porosity, and Structure. In *Asteroids III*, edited by W. F. Bottke Jr., A. Cellino, P. Paolicchi, and R. P. Binzel, 485–500. Tucson, Arizona: University of Arizona Press.
- Browning, L. B., McSween Jr., H. Y., and Zolensky, M. E. 1996. Correlated Alteration Effects in CM Carbonaceous Chondrites. *Geochimica et Cosmochimica Acta* 60: 2621–33.
- Bruckman, V. J. and Wriessnig, K. 2013. Improved Soil Carbonate Determination by FT-IR and X-Ray Analysis. *Environmental Chemistry Letters* 11: 65–70.
- Busemann, H., Alexander, M. O., and Nittler, L. R. 2007. Characterization of Insoluble Organic Matter in Primitive Meteorites by MicroRaman Spectroscopy. *Meteoritics & Planetary Science* 42: 1387.
- Cambioni, S., Delbo, M., Poggiali, G., Avdellidou, C., Ryan, A. J., Deshapriya, J. D. P., Asphaug, E. et al. 2021. Fine-Regolith Production on Asteroids Controlled by Rock Porosity. *Nature* 598: 49–52.
- Changela, H. G., Le Guillou, C., Bernard, S., and Brearley, A. J. 2018. Hydrothermal Evolution of the Morphology, Molecular Composition, and Distribution of Organic Matter in CR (Renazzo-Type) Chondrites. *Meteoritics & Planetary Science* 53: 1006–29.
- Chizmadia, L. J. and Brearley, A. J. 2008. Mineralogy, Aqueous Alteration, and Primitive Textural Characteristics of Fine-Grained Rims in the Y-791198 CM2 Carbonaceous Chondrite: TEM Observations and Comparison to ALHA81002. *Geochimica et Cosmochimica Acta* 72: 602–25.
- Cloutis, E. A., Hudon, P., Hiroi, T., Gaffey, M. J., and Mann, P. 2011. Spectral Reflectance Properties of Carbonaceous Chondrites: 2. CM Chondrites. *Icarus* 216: 309–46.
- Consolmagno, G. J., Britt, D. T., and Macke, R. J. 2008. The Significance of Meteorite Density and Porosity. *Chemie der Erde* 68: 1.
- Corrigan, C. M., Zolensky, M. E., Dahl, J., Long, M., Weir, J., Sapp, C., and Burkett, P. J. 1997. The Porosity and Permeability of Chondritic Meteorites and Interplanetary Dust Particles. *Meteoritics* 32: 509–16.
- Davidson, J., Alexander, C. M. O'D., Bates, H. C., King, A. J., Foustoukos, D. I., Schrader, D. L., Bullock, E. S. et al. 2020. Coordinated Studies of Samples Relevant for Carbonaceous Asteroid Sample Return: CM Chondrites AZ and Meteorite Hills 00639 (Abstract #1623). 51st Lunar and Planetary Science Conference. CD-ROM
- Davison, T. M., Collins, G. S., and Bland, P. A. 2016. Mesoscale Modeling of Impact Compaction of Primitive Solar System Solids. *The Astrophysical Journal* 821: 68.
- De Gregorio, B. T., Stroud, R. M., Nittler, L. R., Alexander, C. M. O'D., Bassim, N. D., Cody, G. D., Kilcoyne, A. L. D. et al. 2013. Isotopic and Chemical Variation of Organic Nanoglobules in Primitive Meteorites. *Meteoritics & Planetary Science* 48: 904–28.
- De Leuw, S., Rubin, A. E., and Wasson, J. T. 2010. Carbonates in CM Chondrites: Complex Formational Histories and Comparison to Carbonates in CI Chondrites. *Meteoritics & Planetary Science* 45: 513–30.
- DeCarli, P. S., Bowden, E., and Seaman, L. 2001. Shock Induced Compaction and Porosity in Meteorites (Abstract). *Meteoritics & Planetary Science* 36: A47.
- Delbo, M., Libourel, G., Wilkerson, J., Murdoch, N., Michel, P., Ramesh, K. T., Ganino, C., Verati, C., and Marchi, S. 2014. Thermal Fatigue as the Origin of Regolith on Small Asteroids. *Nature* 508: 233–6.
- DellaGiustina, D. N., Kaplan, H. H., Simon, A. A., Bottke, W. F., Avdellidou, C., Delbo, M., Ballouz, R.-L. et al. 2021. Exogenic Basalt on Asteroid (101955) Bennu. *Nature Astronomy* 5: 31–8.
- Dionnet, Z., Aléon-Toppani, A., Baklouti, D., Borondics, F., Brisset, F., Djouadi, Z., Sandt, C., and Brunetto, R. 2018. Organic and Mineralogic Heterogeneity of the Paris Meteorite Followed by FTIR Hyperspectral Imaging. *Meteoritics & Planetary Science* 53: 2608–23.
- Dionnet, Z., Brunetto, R., Aléon-Toppani, A., Rubino, S., Baklouti, D., Borondics, F., Buellet, A. C. et al. 2020. Combining IR and X-Ray Micro-Tomography Data Sets: Application to Itokawa Particles and to Paris Meteorite. *Meteoritics & Planetary Science* 55: 1645–64.
- Dionnet, Z., Suttle, M., Longobardo, A., Folco, L., Rotundi, A., Della, C. V., and King, A. 2020. X-Ray Computed Tomography: Morphological and Porosity Characterization of Giant Antarctic Micrometeorites. *Meteoritics & Planetary Science* 55: 1581–99.

- Ebel, D. S. and Rivers, M. L. 2007. Meteorite 3-D Synchrotron Microtomography: Methods and Applications. *Meteoritics & Planetary Science* 42: 1627.
- Feng, H., Jones, K. W., Tomov, S., Stewart, B., Herzog, G. F., Schnabel, C., and Brownlee, D. E. 2005. Internal Structure of Type I Deep-Sea Spherules by X-Ray Computed Microtomography. *Meteoritics & Planetary Science* 40: 195–206.
- Floss, C., Le Guillou, C., and Brearley, A. J. 2014. Coordinated NanoSIMS and FIB-TEM Analyses of Organic Matter and Associated Matrix Materials in CR3 Chondrites. *Geochimica et Cosmochimica Acta* 139: 1–25.
- Forman, L. V., Bland, P. A., Timms, N. E., Daly, L., Benedix, G. K., Trimby, P. W., Collins, G. S., and Davison, T. M. 2017. Defining the Mechanism for Compaction of the CV Chondrite Parent Body. *Geology* 45: 559–62.
- Friedrich, J. M., Ruzicka, A., Macke, R. J., Thostenson, J. O., Rudolph, R. A., Rivers, M. L., and Ebel, D. S. 2017. Relationships Among Physical Properties as Indicators of High Temperature Deformation or Post-Shock Thermal Annealing in Ordinary Chondrites. *Geochimica et Cosmochimica Acta* 203: 157–74.
- Gattacceca, J., McCubbin, F. M., Bouvier, A., and Grossman, J. N. 2019. The Meteoritical Bulletin, No. 108. *Meteoritics & Planetary Science* 55: 1146–50.
- Genge, M. J., Suttle, M., and Van Ginneken, M. 2017. Thermal Shock Fragmentation of Mg Silicates Within Scoriaceous Micrometeorites Reveal Hydrated Asteroidal Sources. *Geology* 45: 891–4.
- Glavin, D. P., Elsila, J. E., McLain, H. L., Aponte, J. C., Parker, E. T., Dworkin, J. P., Hill, D. H., Connolly, H. C., and Lauretta, D. S. 2021. Extraterrestrial Amino Acids and L-Enantiomeric Excesses in the CM2 Carbonaceous Chondrites AZ and Murchison. *Meteoritics & Planetary Science* 56: 148–73.
- Grady, M. M., Graham, A. L., Barber, D. J., Aylmer, D., Kurat, G., Ntafos, T., Ott, U., Palme, H., and Spettel, B. 1987. Yamato-82042: An Unusual Carbonaceous Chondrite with CM Affinities. *Memoirs of the National Institute of Polar Research (Tokyo)* 46: 162–78.
- Griffin, L. D., Elangovan, P., Mundell, A., and Hezel, D. C. 2012. Improved Segmentation of Meteorite Micro-CT Images Using Local Histograms. *Computers & Geosciences* 39: 129–34.
- Hamilton, V. E. 2010. Thermal Infrared (Vibrational) Spectroscopy of Mg-Fe Olivines: A Review and Applications to Determining the Composition of Planetary Surfaces. *Chemie der Erde—Geochemistry* 70: 7–33.
- Hamilton, V. E., Christensen, P. R., Kaplan, H. H., Haberle, C. W., Rogers, A. D., Glotch, T. D., Breitenfeld, L. B. et al. 2021. Evidence for Limited Compositional and Particle Size Variation on Asteroid (101955) Bennu from Thermal Infrared Spectroscopy. *Astronomy & Astrophysics* 650: A120.
- Hamilton, V. E., Simon, A. A., Christensen, P. R., Reuter, D. C., Clark, B. E., Barucci, M. A., Bowles, N. E. et al., OSIRIS-REX Team. 2019. Evidence for Widespread Hydrated Minerals on Asteroid (101955) Bennu. *Nature Astronomy* 3: 332–40. <https://doi.org/10.1038/s41550-019-0722-2>.
- Hanna, R. D., Hamilton, V. E., Haberle, C. W., King, A. J., Abreu, N. M., and Friedrich, J. M. 2020. Distinguishing Relative Aqueous Alteration and Heating Among CM Chondrites with IR Spectroscopy. *Icarus* 346: 113760. <https://doi.org/10.1016/j.icarus.2020.113760>.
- Hanna, R. D., Ketcham, R. A., Zolensky, M., and Behr, W. M. 2015. Impact-Induced Brittle Deformation, Porosity Loss, and Aqueous Alteration in the Murchison CM Chondrite. *Geochimica et Cosmochimica Acta* 171: 256–82.
- Hanowski, N. P. and Brearley, A. J. 2001. Aqueous Alteration of Chondrules in the CM Carbonaceous Chondrite, Allan Hills 81002: Implications for Parent Body Alteration. *Geochimica et Cosmochimica Acta* 65: 495–518.
- Hewins, R. H., Bourot-Denise, M., Zanda, B., Leroux, H., Barrat, J.-A., Humayun, M., Göpel, C. et al. 2014. The Paris Meteorite, the Least Altered CM Chondrite So Far. *Geochimica et Cosmochimica Acta* 124: 190–222.
- Hezel, D. C., Elangovan, P., Viehmann, S., Howard, L., Abel, R. L., and Armstrong, R. 2013. Visualisation and Quantification of CV Chondrite Petrography Using Micro-tomography. *Geochimica et Cosmochimica Acta* 116: 33–40.
- Hicks, L. J. and Bridges, J. C. 2020. Aqueous Alteration in the CM2 AZ Meteorite (Abstract #2869). 51st Lunar and Planetary Science Conference. CD-ROM.
- Hofmeister, A. M. and Pitman, K. M. 2007. Evidence for Kinks in Structural and Thermodynamic Properties Across the Forsterite-Fayalite Binary from Thin-film IR Absorption Spectra. *Physics and Chemistry of Minerals* 34: 319–33.
- Howard, K. T., Alexander, C., Schrader, D. L., and Dyl, K. A. 2015. Classification of Hydrous Meteorites (CR, CM and C2 Ungrouped) by Phyllosilicate Fraction: PSD-XRD Modal Mineralogy and Planetesimal Environments. *Geochimica et Cosmochimica Acta* 149: 206–22.
- Isa, J., Orthous-Daunay, F. R., Beck, P., Herd, C. D., Vuitton, V., and Flandinet, L. 2021. Aqueous Alteration on Asteroids Simplifies Soluble Organic Matter Mixtures. *The Astrophysical Journal Letters* 920: 39.
- Kebukawa, Y., Alexander, C. M. O'D., and Cody G. D. 2011. Compositional Diversity in Insoluble Organic Matter in Type 1, 2 and 3 Chondrites as Detected by Infrared Spectroscopy. *Geochimica et Cosmochimica Acta* 75: 3530–41.
- Kebukawa, Y., Zolensky, M. E., Mathurin, J., Dartois, E., Engrand, C., Duprat, J., Deniset-Besseau, A. et al. 2020. Organic Matter in the AZ (CM2) Meteorite: High Abundance of Aliphatic Carbon in Metal-Rich Lithology (Abstract #1349). 51st Lunar and Planetary Science Conference. CD-ROM.
- Kerraouch, I., Bischoff, A., Zolensky, M. E., Pack, A., Patzek, M., Hanna, R. D., Fries, M. D. et al. 2021. The Polymict Carbonaceous Breccia AZ: A Potential Analog to Samples Being Returned by the OSIRIS REX and Hayabusa2 Missions. *Meteoritics & Planetary Science* 56: 277–310.
- Ketcham, R. A. 2005. Three-Dimensional Grain Fabric Measurements Using High-Resolution X-Ray Computed Tomography. *Journal of Structural Geology* 27: 1217–28.
- Ketcham, R. A. and Ryan, T. 2004. Quantification and Visualization of Anisotropy in Trabecular Bone. *Journal of Microscopy* 213: 158–71.
- Kitazato, K., Milliken, R. E., Iwata, T., Abe, M., Ohtake, M., Matsuura, S., Arai, T. et al. 2019. The Surface Composition of Asteroid 162173 Ryugu from Hayabusa 2 Near-Infrared Spectroscopy. *Science* 364: 272–5.

- Kouvatsis, I. and Cartwright, J. A. 2020. The AZ Meteorite: A Review of Chondrules and Fine-Grained Rims Observed Within a New Carbonaceous Chondrite (CM2). *Fall* 51: 2512.
- Lantz, C., Brunetto, R., Barucci, M. A., Dartois, E., Duprat, J., Engrand, C., Godard, M., Ledu, D., and Quirico, E. 2015. Ion Irradiation of the Murchison Meteorite: Visible to Mid-Infrared Spectroscopic Results. *Astronomy & Astrophysics* 577: 1–9.
- Lantz, C., Brunetto, R., Barucci, M. A., Fornasier, S., Baklouti, D., Bourçois, J., and Godard, M. 2017. Ion Irradiation of Carbonaceous Chondrites: A New View of Space Weathering on Primitive Asteroids. *Icarus* 285: 43–57.
- Le Guillou, C., Bernard, S., Brearley, A. J., and Remusat, L. 2014. Evolution of Organic Matter in Orgueil, Murchison and Renazzo During Parent Body Aqueous Alteration: In Situ Investigations. *Geochimica et Cosmochimica Acta* 131: 368–92.
- Lee, M. R. and Lindgren, P. 2016. Aqueous Alteration of Chondrules from the Murchison CM Carbonaceous Chondrite: Replacement, Pore Filling, and the Genesis of Polyhedral Serpentine. *Meteoritics & Planetary Science* 51: 1003–21.
- Lee, M. R., Lindgren, P., and Sofo, M. R. 2014. Aragonite, Breunnerite, Calcite and Dolomite in the CM Carbonaceous Chondrites: High Fidelity Recorders of Progressive Parent Body Aqueous Alteration. *Geochimica et Cosmochimica Acta* 144: 126–56.
- Leroux, H., Marinova, M., Jacob, D., Hewins, R., Zanda, B., Humayun, M., and Lorand, J. P. 2015. A TEM Study of the Fine-Grained Material of the NWA 7533 Martian Regolith Breccia (Abstract #7533). 46th Lunar and Planetary Science Conference. CD-ROM.
- Lewis, J. A., Jones, R. H., and Garcea, S. C. 2018. Chondrule Porosity in the L4 Chondrite Saratov: Dissolution, Chemical Transport, and Fluid Flow. *Geochimica et Cosmochimica Acta* 240: 293–313.
- Lindgren, P., Hanna, R. D., Dobson, K. J., Tomkinson, T., and Lee, M. R. 2015. The Paradox Between Low Shock-Stage and Evidence for Compaction in CM Carbonaceous Chondrites Explained by Multiple Low-Intensity Impacts. *Geochimica et Cosmochimica Acta* 148: 159–78.
- Macke, R. J., Consolmagno, G. J., and Britt, D. T. 2011. Density, Porosity, and Magnetic Susceptibility of Carbonaceous Chondrites. *Meteoritics & Planetary Science* 46: 1842–62.
- Martin, P. M. C. and Lee, M. R. 2020. Degree of Aqueous Alteration of the CM Carbonaceous Chondrite AZ: Implications for Understanding Ryugu and Bennu (Abstract #1375). 51st Lunar and Planetary Science Conference. CD-ROM.
- Matrajt, G., Messenger, S., Brownlee, D., and Joswiak, D. 2012. Diverse Forms of Primordial Organic Matter Identified in Interplanetary Dust Particles. *Meteoritics & Planetary Science* 47: 525–49.
- Matsumoto, M., Tsuchiyama, A., Nakato, A., Matsuno, J., Miyake, A., Kataoka, A., Ito, M. et al. 2019. Discovery of Fossil Asteroidal Ice in Primitive Meteorite Acfer 094. *Science Advances* 5: 5078.
- Merouane, S., Djouadi, Z., Le Sergeant d’Hendecourt, L., Zanda, B., and Borg, J. 2012. Hydrocarbon Materials of Likely Interstellar Origin from the Paris Meteorite. *The Astrophysical Journal* 756: 154.
- Metzler, K., Bischoff, A., and Stöffler, D. 1992. Accretionary Dust Mantles in CM Chondrites: Evidence for Solar Nebula Processes. *Geochimica et Cosmochimica Acta* 56: 2873–97.
- Michel, P., Ballouz, R. L., Barnouin, O. S., Jutzi, M., Walsh, K. J., May, B. H., Manzoni, C. et al. 2020. Collisional Formation of Top-Shaped Asteroids and Implications for the Origins of Ryugu and Bennu. *Nature* 11: 2655.
- Mirone, A., Brun, E., Gouillart, E., Tafforeau, P., and Kieffer, J. 2014. The PyHST2 Hybrid Distributed Code for High Speed Tomographic Reconstruction with Iterative Reconstruction and A Priori Knowledge Capabilities. *Nuclear Instrument Methods Physical Research, Section B* 324: 41.
- Nakamura-Messenger, K., Messenger, S., Keller, L. P., Clemett, S. J., and Zolensky, M. E. 2006. Organic Globules in the Tagish Lake Meteorite: Remnants of the Protosolar Disk. *Science* 5804: 1439–42.
- Noun, M., Baklouti, D., Brunetto, R., Borondics, F., Calligaro, T., Dionnet, Z., Le Sergeant d’Hendecourt, L. et al. 2019. A Mineralogical Context for the Organic Matter in the Paris Meteorite Determined by a Multi-Technique Analysis. *Life* 9: 44.
- Okada, T., Fukuhara, T., Tanaka, S., Taguchi, M., Arai, T., Senshu, H., Sakatani, N. et al. 2020. Highly Porous Nature of a Primitive Asteroid Revealed by Thermal Imaging. *Nature* 579: 518–22.
- Paganin, D., Mayo, S. C., Gureyev, T. E., Miller, P. R., and Wilkins, S. W. 2002. Simultaneous Phase and Amplitude Extraction from a Single Defocused Image of a Homogeneous Object. *Journal of Microscopy* 206: 33.
- Pilorget, C., Okada, T., Hamm, V., Brunetto, R., Yada, T., Loizeau, D., Riu, L. et al. 2021. First Compositional Analysis of Ryugu Samples by the MicrOmega Hyperspectral Microscope. *Nature Astronomy* 6: 221–5. <https://doi.org/10.1038/s41550-021-01549-z>.
- Pizzarello, S., Yarnes, C. T., and Cooper, G. 2020. The AZ (CM2) Meteorite: New Insights into Early Solar System Organic Chemistry. *Meteoritics & Planetary Science* 55: 1525–38.
- Potin, S., Beck, P., Bonal, L., Schmitt, B., Garenne, A., Moynier, F., Agranier, A., Schmitt-Kopplin, P., Malik, A. K., and Quirico, E. 2020. Mineralogy, Chemistry, and Composition of Organic Compounds in the Fresh Carbonaceous Chondrite Mukundpura: CM1 or CM2? *Meteoritics & Planetary Science* 55: 1681–96.
- Quirico, E., Moroz, L. V., Schmitt, B., Arnold, G., Faure, M., Beck, P., Bonal, L. et al. 2014. Origin of Insoluble Organic Matter in Type 1 and 2 Chondrites: New Clues, New Questions. *Geochimica et Cosmochimica Acta* 136: 80–99.
- Rubin, A. E., Trigo-Rodriguez, J. M., Huber, H., and Wasson, J. T. 2007. Progressive Aqueous Alteration of CM Carbonaceous Chondrites. *Geochimica et Cosmochimica Acta* 71: 2361–82.
- Salisbury, J. W., D’Aria, D. M., and Jarosewich, E. 1991. Mid Infrared (2.5–13.5  $\mu\text{m}$ ) Reflectance Spectra of Powdered Stony Meteorites. *Icarus* 92: 280–97.
- Sandt, C., Dionnet, Z., Toplak, M., Fernandez, E., Brunetto, R., and Borondics, F. 2019. Performance Comparison of Aperture-Less and Confocal Infrared Microscopes. *Journal of Spectral Imaging* 8: 1–14.
- Suttle, M. D., King, A. J., Schofield, P. F., Bates, H., and Russell, S. S. 2021. The Aqueous Alteration of CM Chondrites, a Review. *Geochimica et Cosmochimica Acta* 299: 219–56.
- Takir, D., Howard, K. T., Stockstill-Cahill, K. R., Hibbitts, C. A., Abreu, N., Zolensky, M. E., and Fries, M. 2020.



- Spectroscopy and Mineralogy of Aguas Zarcas (Abstract #2533). 51st Lunar and Planetary Science Conference. CD-ROM.
- Tarantino, S. C., Carpenter, M. A., and Domeneghetti, M. C. 2003. Strain and Local Heterogeneity in the Forsterite-Fayalite Solid Solution. *Physics and Chemistry of Minerals* 30: 495–502.
- Tomeoka, K., Kojima, H., and Yanai, K. 1989. Yamato-86720: A CM Carbonaceous Chondrite Having Experienced Extensive Aqueous Alteration and Thermal Metamorphism. *Proceedings of the NIPR Symposium on Antarctic Meteorites* 2: 55–74.
- Trigo-Rodríguez, J. M., Rubin, A. E., and Wasson, J. T. 2006. Non-Nebular Origin of Dark Mantles Around Chondrules and Inclusions in CM Chondrites. *Geochimica et Cosmochimica Acta* 70: 1271–90.
- Tunney, L. D., Hill, P. J. A., Herd, C. D. K., and Hilts, R. W. 2020. Distinguishing Between Terrestrial and Extraterrestrial Organic Compounds in the CM2 AZ Carbonaceous Chondrite (Abstract #1795). 51st Lunar and Planetary Science Conference. CD-ROM.
- Velbel, M. A., Tonui, E. K., and Zolensky, M. E. 2012. Replacement of Olivine by Serpentine in the Carbonaceous Chondrite Nogoya (CM2). *Geochimica et Cosmochimica Acta* 87: 117–35.
- Velbel, M. A., Tonui, E. K., and Zolensky, M. E. 2015. Replacement of Olivine by Serpentine in the Queen Alexandra Range 93005 Carbonaceous Chondrite (CM2): Reactant-Product Compositional Relations, and Isovolumetric Constraints on Reaction Stoichiometry and Elemental Mobility During Aqueous Alteration. *Geochimica et Cosmochimica Acta* 148: 402–25.
- Villalon, K. L., Heck, P. R., Keating, K., Davis, A. M., and Stephan, T. 2020. GEMS-Like Material in Aguas Zarcas Interchondrule Matrix (Abstract #2757). 51st Lunar and Planetary Science Conference. CD-ROM.
- Vinogradoff, V., Le Guillou, C., Bernard, S., Binet, L., Cartigny, P., Brearley, A. J., and Remusat, L. 2017. Paris vs. Murchison: Impact of Hydrothermal Alteration on Organic Matter in CM Chondrites. *Geochimica et Cosmochimica Acta* 212: 234–52.
- Walsh, K. J., Ballouz, R. L., Bottke, W. F., Avdellidou, C., Connolly, H. C., Delbo, M., DellaGiustina, D. N., et al. 2020. Likelihood for Rubble-Pile Near-Earth Asteroids to be 1st or nth Generation: Focus on Bennu and Ryugu (Abstract #2253). 51st Lunar and Planetary Science Conference. CD-ROM.
- Weisberg, M. K., McCoy, T. J., and Krot, A. N. 2006. Systematics and Evaluation of Meteorite Classification. In *Meteorites and the Early Solar System II*, edited by D. S. Lauretta, and H. Y. McSween Jr., 19–52. Tucson, Arizona: University of Arizona Press.
- Weitkamp, T., Scheel, M., Giorgetta, J., Joyet, V., Roux, V. L., Cauchon, G., Moreno, T., Polack, F., Thompson, A., and Samama, J. 2017. The Tomography Beamline ANATOMIX at Synchrotron SOLEIL. *Journal of Physics: Conference Series* 849: 012037.
- Wells, M., Pel, J. W., Alistair, G., Wright, G. S., Aitink-Kroes, G., Azzollini, R., Beard, S. et al. 2015. The Mid-Infrared Instrument for the James Webb Space Telescope, VI: The Medium Resolution Spectrometer. *The Astronomical Society of the Pacific* 127: 646–64.
- Yada, T., Abe, M., Okada, T., Yogata, K., Miyazaki, A., Hatakeda, K., Kumagai, K. et al. 2021. Preliminary Analysis of the Hayabusa2 Samples Returned from C-Type Asteroid Ryugu. *Nature Astronomy* 6: 214–20.
- Yang, X., Hanna, R. D., Davis, A. M., Neander, A. I., and Heck, P. R. 2021. A Possible Record of an Active Asteroid: Discovery of a Compact Lithology in the AZ CM Chondrite (Abstract #6075). 84th Annual Meeting of the Meteoritical Society.
- Yesiltas, M., Sedlmair, J., Peale, R. E., and Hirschmugl, C. J. 2016. Synchrotron-Based Three-Dimensional Fourier Transform Infrared Spectro-Microtomography of Murchison Meteorite Grain. *Applied Spectroscopy* 71: 1198–208.
- Zanetta, P.-M., Leroux, H., Le Guillou, C., Zanda, B., and Hewins, R. H. 2021. Nebular Thermal Processing of Accretionary Fine-Grained Rims in the Paris CM Chondrite. *Geochimica et Cosmochimica Acta* 295: 135–54.
- Zolensky, M. E., Mittlefehldt, D. W., Lipschutz, M. E., Wang, M. S., Clayton, R. N., Mayeda, T. K., Grady, M. M., Pillinger, C., and David, B. 1997. CM Chondrites Exhibit the Complete Petrologic Range from Type 2 to 1. *Geochimica et Cosmochimica Acta* 61: 5099–115.
-